Two-photon Microscopy and Polarimetry for Assessment of Myocardial Tissue Organization

by

Marika Archambault-Wallenburg

A thesis submitted in conformity with the requirements
for the degree of Master of Science
Graduate Department of Medical Biophysics
University of Toronto

Your file Votre référence
ISBN:978-0-494-72497-2
Our file Notre référence
ISBN: 978-0-494-72497-2

Abstract

Two-photon Microscopy and Polarimetry for Assessment of Myocardial Tissue Organization

Marika Archambault-Wallenburg

Master of Science

Graduate Department of Medical Biophysics

University of Toronto

2010

Optical methods can provide useful tissue characterization tools. For this project, two-photon microscopy and polarized light examinations (polarimetry) were used to assess the organizational state of myocardium in healthy, infarcted, and stem-cell regenerated states. Two-photon microscopy visualizes collagen through second-harmonic generation and myocytes through two-photon excitation autofluorescence, providing information on the composition and structure/organization of the tissue. Polarimetry measurements yield a value of linear retardance that can serve as an indicator of tissue anisotropy, and with a dual-projection method, information about the anisotropy axis orientation can also be extracted. Two-photon microscopy results reveal that stem-cell treated tissue retains more myocytes and structure than infarcted myocardium, while polarimetry findings suggest that the injury caused by temporary ligation of a coronary artery is less severe and more diffuse that than caused by a permanent ligation. Both these methods show potential for tissue characterization.

Acknowledgements

I am grateful to my supervisor, Alex Vitkin, for his guidance, advice and support over the past two years. I would also like to thank my committee members Lothar Lilge and Ren-Ke Li for their feedback and useful suggestions. Finally, I extend my thanks to Mike Wood and Nirmalya Ghosh, as well as to Mihaela Pop and Jun Wu, for their help and insight with various aspects of this work.

Support for this work was provided by the Natural Sciences and Engineering Research Council, the Canadian Foundation for Innovation, and the Canadian Institutes of Health Research.

Contents

List of Tables

List of Figures

List of Symbols and Abbreviations

α	Rotation between two imaging planes (dual-projection reconstruction), see Fig. 4.2
β	Angle error (dual-projection reconstruction), page 48
χ	Off-axis angle of incident beam arm (polarimetry setup), see Fig. 3.2
χ_2	Second-order non-linear susceptibility, page 6
$\Delta\delta'$	Relative deviation of the reconstructed linear retardance (dual projection reconstruction), page 48
Δn	Birefringence, page 8
Δn_{app}	Apparent birefringence, see equation (3.2)
δ	Linear retardance, see equation (1.1)
δ'	Reconstructed linear retardance, see equation (4.3)
δ_{app}	Apparent linear retardance, see equation (3.1)
ϵ_0	Permittivity of free space, page 6
$\hbar$	Reduced Planck constant, page 5
λ	Wavelength

λ_{em}	Emission wavelength
λ_{ex}	Excitation wavelength
$\mathbf{M_D}$	Diattenuation matrix, page 31
$\mathbf{M_R}$	Retarder matrix, page 31
$\mathbf{M_\Delta}$	Depolarization matrix, page 31
$\mathbf{M}_\psi$	Circular retardance matrix, page 32
$\mathbf{M_{LR}}$	Linear retardance matrix, page 32
$\mathbf{M}$	Mueller matrix, page 26
ω_0	Incident photon frequency, page 5
θ	Azimuthal angle of anisotropy axis, see Fig. 3.1
φ	Elevation angle of anisotropy axis, see Fig. 3.1
$\mathbf{E}$	Electric field, page 5
$\mathbf{P}$	Induced polarization, page 5
$\mathbf{S}$	Stokes vector, page 26
d	Pathlength of light
F	Ratio between the apparent and real birefringence, see equation (4.2)
I	Stokes parameter: total intensity, page 26
n	Apparent index of refraction, see equation (3.3)
n_e	Index of refraction for polarizations parallel to the extraordinary axis, page 8

n_o	Index of refraction for polarizations perpendicular to the extraordinary axis, page 8
Q	Stokes parameter: vertical/horizontal polarization, page 26
U	Stokes parameter: $\pm 45^\circ$ polarization, page 26
V	Stokes parameter: circular polarization, page 26
A	Polarization analyzer, page 29
CCD	Charge-coupled device, page 29
DT-MRI	Diffusion-tensor magnetic resonance imaging, page 56
FA	Fractional anisotropy, as determined by DT-MRI, see equation (5.1)
IR	Ischemia / Reperfusion, page 34
L	Lens, page 29
LAD	Left anterior descending (coronary artery), page 14
LV	Left ventricle
MI	Myocardial infarction, page 34
MRI	Magnetic resonance imaging
QWP	Quarter-wave plate, page 29
RV	Right ventricle
SHG	Second-harmonic generation, page 4
TPEF	Two-photon excitation fluorescence, page 4
TPM	Two-photon microscopy, page 4

Chapter 1

Introduction

1.1 Myocardial infarction

Cardiovascular diseases are the most common cause of death in the developed world. In particular, myocardial infarctions (also known as heart attacks), which occur when blood supply to part of the myocardium is interrupted, are the cause of many of these deaths (over 17,000 annually in Canada only[1]). The one-year survival after a myocardial infarction is roughly 95%[1], with many of these patients experiencing progressive heart failure. There is therefore a pressing need for therapies which maintain or restore heart function after myocardial infarction, and correspondingly a need to assess these therapies whether in animal models of disease and treatment, or in patients.

Myocardial infarction occurs when part of the heart muscle is deprived of blood, often as the result of thrombus caused by the rupture of an atherosclerotic plaque. This results in the death, by apoptosis and necrosis, of myocardial cells, including contractile muscle cells which occupy roughly 75% of the volume of the healthy heart[2]. In healthy myocardium, collagen of type I (the most common type) forms thick fibers, and is normally produced very slowly by fibroblasts and smooth muscle cells[3], while collagen type

III (which represents 10 percent of total heart collagen content) forms thinner fibers. After an infarct, significant amounts of collagen I and III are secreted within two to three days. The final scar, formed after several weeks, is constituted of type I (40%), type III (35%) and type V (25%) collagen[3]. The accumulation of collagen increases the wall stiffness, disrupts normal electrical conduction within the heart, generates arrhythmias, and reduces the efficacy of blood pumping by making the myocardium heterogeneous (non-uniform contractility). The infarct expands and thins out because of the death and slippage of the myocytes, while the non-infarct region thickens due to increased stress, inducing ventricular remodeling and causing the double-spiral structure of the heart to be perturbed[3]. Both the disruption of the normal alignment of muscle fibers (which normally form a double-spiral structure) and the replacement of muscle tissue by patches of non-contractile scar tissue reduce the heart functionality by interfering with its normal contractile function[4,5].

One of the approaches that has been investigated to prevent cardiac dysfunction in patients who have suffered a myocardial infarction is cell therapy. Animal studies have shown that implantation of stem cells in the damaged tissue (even when delayed until 30 days after infarct) can increase cardiac function and prevent progressive ventricular dilation[6,7,8]. A variety of cell types have been studied[6,9], including hematopoietic stem cells[10,11], mesenchymal stem cells[12,13,14], cardiac stem cells[15], skeletal myoblasts[8,16], and embryonic stem cells[17]. Hematopoeitic stem cells, mesenchymal stem cells, and cardial stem cells all have the potential to differentiate into myogenic cells, which can produce new cardiomyocytes, smooth muscle cells, and vascular endothelial cells[6]. Mesenchymal stem cells are easy to access[6] and appear to go undetected by the immune system of the host[9,18], which has obvious clinical benefits. The mechanism of cardiac function improvement by stem cells is not clear, as it has been shown that very few of the implanted stem cells differentiate into cardiomytes[7,19]. It is thought that functional improvement is

mediated by paracrine effects of the implanted cells on the host myocardium[7], including decreases apoptosis, increases angiogenesis, and decreases extracellular matrix degradation[8,20,21]. Finally, while cell therapy has had success in animal models, these results have not been translated as successfully in clinical trials[6], with discrepant outcomes in different studies[18]. The underwhelming results achieved in clinical trials may be due to various co-morbidities of the (usually elderly) recipients of cell therapy, or to the reduced regenerative capacity of the patient's stem cells (as these were autologous transplants)[6]. There is therefore a need to determine the optimal parameters for stem cell therapy (e.g. type of implanted cells, method of delivery) in appropriate animal models of ischemic injury[18]. Occlusion of a major coronary artery, either permanent or followed by reperfusion, has been found to be a good animal model to study myocardial ischemia, with the reperfusion model presenting a markedly stronger inflammatory response[22].

Acurate assessment of myocardial tissue organization is important for both pre-clinical evaluation of novel therapies and for clinical treatment of myocardial infarction patients in order to i) to properly understand the effects of stem cell regeneration, and ii) to evaluate and improve treatments. Currently, cardiovascular ultrasound is commonly used to assess heart function in patients[23], nuclear imaging techniques such as SPECT are routinely used to diagnose myocardial infarcts[24] and cardiac magnetic resonance imaging can be used to detect infarcts that are missed by SPECT because they are not transmural[24]. Finally, electrical and mechanical activity of the heart can be evaluated clinically with electrodes (electrical mapping) or voltage-sensitive dyes (optical mapping)[25,26,27].

In addition to the above-mentioned methods, diffusion tensor MRI[28,29,30,31] (which enables fiber reconstruction through assessment of diffusion anisotropy and direction) and two-photon microscopy[32] (which allows assessment of tissue components through endogenous or exogenous molecules) have been used in animal studies either *in vivo* or

in excised but perfused hearts to visualize heart structure and composition. *Ex vivo*, histology and microscopy are most commonly used to visualize heart composition and structure, though other methods including optical coherence tomography, spontaneous Raman spectroscopy, and polarized-light methods, have shown potential for cardiac tissue assessment: optical coherence tomography[33,34] enables reconstruction of cardiac structures up to 2 mm inside cardiac tissue; spontaneous Raman spectroscopy[35] provides chemical contrast between different cardiac components; and polarimetry[36] can assess tissue composition and structure by evaluating birefringence. This work will focus on the use of two optical methods, two-photon microscopy and polarimetry, to assess myocardial tissue structure.

1.2 Two-photon microscopy

Two-photon microscopy (TPM) has become a widely-used tool in recent years for many applications including cardiac tissue imaging, as it offers many advantages over conventional and confocal microscopy, and histology. While maintaining the high resolution of confocal microscopy, TPM has the added benefits of intrinsic depth-sectioning, no out-of-focus bleaching, and high depth penetration (up to hundreds of microns in certain tissues)[37,38]. Furthermore, many endogenous molecules can serve as sources of signal for TPM, eliminating the need for labels and stains for certain applications. For instance, two-photon excitation autofluorescence (TPEF) allows for imaging of endogenous fluorescent structures such as extracellular matrix (elastin[39,40]) or of cells containing endogenous fluorophores (including NADH, flavins, and others[41]). Second harmonic generation (SHG), another non-linear optical process, is generated by non-centrosymmetric molecules and can be exploited to image well-ordered protein structures such as collagen[39,40,42], microtubules[43] and myosin[44,45,46]. The potential of two-photon microscopy is

well established in cardiology: it has been performed on whole (healthy and diseased) mouse hearts[47,48], on diseased human and porcine heart valve tissues[49], on human atrial myocardium[50], and on perfused ischemic rat hearts[32], though not *in vivo*.

The physical process of two-photon excitation fluorescence is similar to that of single-photon fluorescence, in that it involves the absorption of photon energy by a molecule (the fluorophore) which is promoted to an excited state, and the re-emission of a photon of slightly lower energy as the excited molecule returns to its ground state. Two-photon excitation, however, occurs when not one but two photons are absorbed by the fluorophore within approximately an attosecond (10^{-18} s) of each other[38]. Specifically, energy is tranferred by two photons of energy $\hbar\omega_0$ to promote a molecule to an excited state ($A \rightarrow A^*$), which loses some energy through thermal loss, then re-emits a photon of energy $\hbar\omega < 2\hbar\omega_0$ (see Fig. 1.1a). When the fluorophore is endogenous, this process is called two-photon excitation autofluorescence. TPEF, like other multiphoton processes, requires very high contentrations of photons, and therefore is only produced in the very small focal volume: the effective excitation volume is less than a femtoliter ($1\ \mu m^3$)), where the photon flux is sufficiently high[38] (typically $10^{20} - 10^{30}$ photons/(cm^{2}s). Many endogenous molecules commonly found in cells produce two-photon excitation autofluorescence, making it a useful tool for imaging cells, including myocytes[40,44].

Second-harmonic generation is another non-linear optical process, by which light of frequency $2\omega_0$ is generated from the interaction of light of frequency ω_0 (i.e. half the energy) with non-centrosymmetric molecules (see Fig. 1.1b). As a lightwave travels through a medium, the electromagnetic field exerts a force on the valence electrons of molecules, which shift and create an induced polarization $\mathbf{P}$ that is proportional to the electric field $\mathbf{E}$. If the electric field becomes too high, the linear relationship between $\mathbf{P}$ and $\mathbf{E}$ breaks down and the molecules start behaving like anharmonic oscillators. The

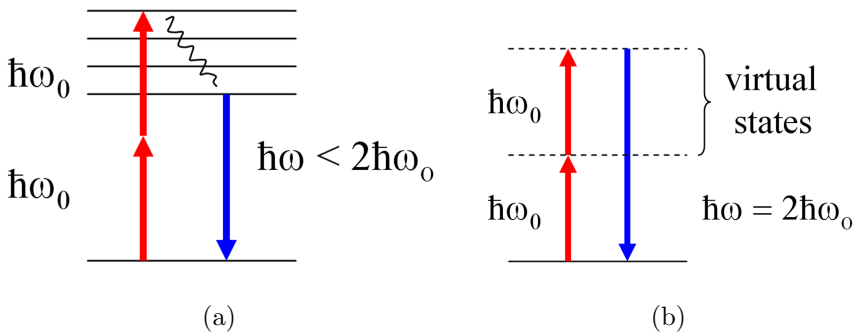

Figure 1.1: Energy-level diagram for (a) two-photon excitation fluorescence and (b) second-harmonic generation.

induced polarization can be expressed as a series expansion with higher-order terms, $\mathbf{P} = \epsilon_0(\chi\mathbf{E} + \chi_2\mathbf{E}^2 + \chi_3\mathbf{E}^3 + ...)$, where χ_2 is the second-order non-linear susceptibility. Because the electric field is a sinusoidal function of time, oscillations at higher frequencies ($2\omega_0$, $3\omega_0$, ...) will be present. If a molecule has inversion symmetry (i.e. incoming fields of $\mathbf{E}(\omega_0)$ and $-\mathbf{E}(\omega_0)$ induce polarizations of $\mathbf{P}(2\omega_0)$ and $-\mathbf{P}(2\omega_0)$ respectively), the even components of the dipole moment $\mathbf{P}$ must vanish (i.e. $\mathbf{P} = \epsilon_0(\chi\mathbf{E} + \chi_3\mathbf{E}^3 + ...)$)[51,52]: second-harmonic generation (but not third-harmonic generation) is therefore precluded. For a non-centrosymmetric molecule however, there is no such conditition, and second-harmonic generation is produced. In biological samples, molecules that satisfy this criterium include collagen, myosin, and tubulin[53]. SHG, like TPEF, requires very high photon concentration.

Because TPEF and SHG have different spectral signatures (for SHG, $\lambda_{em} = 0.5\lambda_{ex}$ while for TPEF, $\lambda_{em} > 0.5\lambda_{ex}$), these two signals can be separated spectrally. In heart tissue, TPEF is produced in cardiomyocytes (which contain NADH, flavins and other fluorophores), and SHG is produced by collagen (which in its fibrillar form is non-centrosymmetric). Two-photon microscopy therefore allows simultaneous imaging of cardiomyocytes and collagen in cardiac tissue and provides insight into tissue composition and organization. Because of the high collagen content of infarcted myocardium

and the importance of this fibrosis on ventricular function, two-photon microscopy is particularly well suited to study myocardial infarction and regeneration.

1.3 Polarimetry

Optical polarimetry provides another way of obtaining a wealth of information about a medium's properties, by analyzing its interactions with polarized light. Historically, polarized light methodologies have not seen extensive use in biomedicine because of severe depolarizing effects caused by multiple scattering. Nevertheless, some research on polarimetric tissue characterization has been reported, for instance in thermally damaged tissues[54,55], in skin for cancer detection[56,57], in articular cartilage[58], in the crystalline lens[59] and in rat myocardium[36,60] using various polarized light parameters which exploit the many interactions of polarized light with matter (e.g. depolarization, birefringence).

When polarized light is transmitted through or reflected from a sample, its polarization state is altered by its interactions with the sample. The polarization of light can be decreased (depolarization), rotated (retardance), different polarization states can be attenuated differently (diattenuation), or all of these effects can occur simultaneously. These processes reflect medium properties that can yield medically relevent information: for instance, optical rotation can serve as a clue to concentration of chiral molecules like glucose, and linear retardance can be used as an indicator of tissue anisotropy. These effects are probed by measuring the output polarization state for different (known) input polarization states. Because so many processes can occur simultaneously, the output polarization states reflect their combined effect, and disentangling the contribution of each process becomes a complex task. Many different strategies have been used to interpret results from polarimetry, including taking the output polarization state directly (in the

form of a 4-element vector called the Stokes vector, the components of which represent the different output polarization states) or at the transfer function of the polarization states (in the form of a 4-by-4 matrix called the Mueller matrix). There are also ways of extracting individual parameters relating to each process (depolarization, retardance, diattenuation) from the Mueller matrix. One such method called Mueller matrix decomposition[61] has been used by our group, and was shown to produce good estimates of the properties of optical phantoms in experiments and in Monte Carlo simulations[62].

Of particular relevance for this work is linear retardance. This is a phase shift that accrues between orthogonal polarizations components as they traverse a material that displays two (or more) different indices of refraction, a property called birefringence. Because birefringence is a reflection of anisotropy of the optical properties of a material, it can be used to assess microstructure and organization in biological tissues: highly aligned molecules and structures (such as linear collagen and myocytes) will exhibit higher birefringence than disorganized structures with little anisotropy (such as scar tissue). Birefringence (and linear retardance, its measurable effect) has been used to characterize tissue in skin[57,63], articular cartilage[64,65] and skeletal and cardiac muscle[36,60,66,67].

Recently, members of our polarimetry group have explored the use of linear retardance measurements (as extracted by Mueller matrix decomposition) to monitor stem cell regenerative treatments of myocardial infarction[36,60], as striated heart tissue will have a higher anisotropy than the scar tissue that replaces it when cell death occurs, and therefore have a larger birefringence. Linear retardance, δ, was used as a measure of birefringence, $\Delta n = n_e - n_o$ (n_e and n_o are the refractive indices for polarizations parallel and perpendicular to the extraordinary axis*, respectively), as the two are proportional:

*The extraordinary axis, or optical axis, is the axis along which velocity will be the same for light polarized in all azimuths. When viewed along its extraordinary axis, an anisotropic substance will appear isotropic.

$$\delta = \frac{2\pi}{\lambda} d\Delta n \tag{1.1}$$

where d is the pathlength of photons and λ is the wavelength of light. It was found that linear retardance decreased in the region of injury, with stem-cell treated hearts showing a less severe decrease in retardance than untreated hearts[60]. These results suggested that optical polarimetry could be a good way to monitor tissue structure after myocardial infarct and regenerative treatment. Thus, in this project, we continue this work and use polarimetry imaging to characterize changes occuring in infarcted and stem-cell treated myocardium.

1.4 Thesis outline

This project was aimed at using two-photon microscopy and polarimetry as tools for assessing myocardial microstructure after infarct and after stem-cell therapy. It was known from previous polarimetry studies that myocardial infarction and stem cell regeneration induce changes in the linear retardance of myocardium, but it was not clear what mechanisms were responsible for these changes.

Using two-photon microscopy helped determine what underlying changes were taking place that could explain the observed polarimetry trends. Two-photon microscopy results are shown and discussed in chapter 2 of this thesis. Simultaneous second-harmonic generation and two-photon excitation autofluorescence allowed visualization of collagen and myocytes in the heart tissue and determination of the nature of differences in tissue composition and structure between healthy, infarcted, and stem-cell treated rat myocardium.

In chapter 3, polarimetry imaging results for myocardial samples from two different

rat models of infarct (permanent versus temporary) are presented, as well as a comparison to two-photon microscopy of the same samples. The comparison to two-photon images made it possible to correlate the composition and structure of the myocardium with linear retardance values, which revealed that two distinct mechanisms (change of composition affecting tissue anisotropy, and change in tissue organization affecting the anisotropy axis direction) were likely contributing to the observed loss of birefringence after infarct.

A method to separate these two contributions to apparent linear retardance was developed and is described in Chapter 4. A dual-projection method is presented to reconstruct the three-dimensional anisotropy axis of tissue, thus providing a way to uncouple the effects of tissue anisotropy and anisotropy axis orientation. This method was then characterized using a birefringent plastic sphere of fixed anisotropy and controlled optical axis orientation.

Chapter 5 presents data from the dual-projection reconstruction in pig samples, specifically the anisotropy axis and magnitude maps. Diffusion tensor magnetic resonance imaging results for these samples are used as an independent measure of anisotropy and comparisons between polarimetry and diffusion tensor MRI are made.

Finally, Chapter 6 offers a summary of the work presented in the previous chapters and a discussion of future directions.

Three first-author journal publications, two contributing-author publications and a conference poster stemmed from this work:

- M. A. Wallenburg, M. Pop, M. F. G. Wood, N. Ghosh, G. A. Wright, and I. A. Vitkin, "Comparison of optical polarimetry and diffusion tensor MR imaging for

assessing myocardial anisotropy," *Journal of Innovative Optical Health Sciences*, **3** (2), 109-121, (2010). [See Chapter 5]

- M. A. Wallenburg, M.Wood, N. Ghosh, and I. A. Vitkin, "Polarimetry-based method to extract geometry independent metrics of tissue anisotropy," *Optics Letters* **35** (15), 2570-2572, (2010). [See Chapter 4]

- M. A. Wallenburg, J. Wu, R.-K. Li, I. A. Vitkin. "Two-photon microscopy of healthy, infarcted and stem-cell treated regenerating heart," *Journal of Biophotonics* (accepted), (2010). [See Chapter 2]

- M. Wood, N. Ghosh, M. A. Wallenburg, S. Li, R. Weisel, B. Wilson, R. K. Li, and I. A. Vitkin, "Polarization birefringence measurements for characterizing the myocardium, including healthy, infarcted, and stem cell treated regenerating cardiac tissues," *Journal of Biomedical Optics* **15** (in press), (2010).

- J. Wu, Z. Sun, S. Li, H. Kuo, G. Michal, S. Basu, G. Chan, E. Madrusov, F. Ludwig, M. Wallenburg, I. A. Vitkin, and R.K. Li, "Comparison of long-term structural and functional outcomes of cardiac ischemia/reperfusion and permanent ligation injuries in rat," (manuscript in preparation), (2010).

- M. A. Wallenburg, M. F. G. Wood, N. Ghosh, M. Pop, J. Wu, R.-K. Li, G. A. Wright, and I. A. Vitkin, "Polarimetry for assessment of myocardial tissue structure". Poster presented at the Gordon Research Conference on Lasers in Medicine and Biology, July 2010. [Best poster award]

Chapter 2

Two-photon microscopy

2.1 Introduction

As described in Section 1.2, two-photon microscopy is particulaly well suited to image infarcted myocardium because of the distinct mechanisms (SHG and TPEF) which allow, through spectral decomposition, simultaneous and intrinsically co-registered visualization of the two main components of infarcted myocardium, namely cardimyocytes and collagen. Myocyte content is key to tissue viability and function, and collagen accumulation plays an important role in the process of adverse remodeling that negatively impacts cardiac function.

Two-photon microscopy was therefore used to image both the collagen and the myocyte content of healthy, infarcted and regenerating (stem-cell treated) rat hearts, yielding structural information on both the extracellular matrix and the muscle cell components of heart. These qualitative results reveal interesting microstructural and compositional features with the potential to verify biological hypotheses regarding the mechanisms of stem cell regeneration*.

*This chapter is based in large part on the results presented in Wallenburg *et al.*[68]

2.2 Methods

2.2.1 Two-photon microscopy

Two-photon microscopy was performed using a Zeiss LSM 510 META NLO microscope. A tunable Chameleon Ti:Sapphire laser (720-930 nm) provided excitation at a wavelength of 840 nm. This wavelength provides strong excitation of second harmonic generation from collagen while minimizing the autofluorescence from collagen. A 20x 0.75 NA dry objective was used for the images presented here. SHG and TPEF signals were recorded in the backscattered direction on a META spectral detector. While TPEF is emitted isotropically, SHG is preferentially emitted in the forward direction, though some signal is also produced in the backscatter direction (more on this in Section 2.4.1). SHG signal was recorded between 400-430 nm (displayed in green pseudocolor). The images produced by TPEF collected over different wavelength ranges (430-460 nm, 460-490 nm, 490-520 nm) change very little. Because the gain for the two collection bands could not be adjusted independently, the 430-460 nm detection range was used for fluorescence (displayed in red pseudocolor) as it yielded a fluorescence intensity which was comparable to the intensity of the SHG signal from the 400-430 nm range. Each 1024 x 1024 pixel (460 μm x 460 μm) region took 31 seconds to scan, with each line averaged 8 times to increase signal-to-noise ratio. Multiple images were tiled to create the larger fields of view in Figs. 2.3-2.5.

2.2.2 Rat heart infarct/regeneration model

All animal studies were performed at the Toronto General Hospital under the lead of Dr. Ren-Ke Li's group and carried out under institutional approval from the University

Health Network. Cardiac samples from a Lewis rat model of myocardial infarction were used. The first group of rats (n=5) underwent permanent ligation of the left anterior descending (LAD) coronary artery, and the animals were sacrificed nine weeks post ligation (see Table 2.1). The second group (n = 4) underwent the same coronary ligation, but were treated one week later with mesenchymal stem cells harvested from bone marrow and transfected with the human elastin gene, administered by intramyocardial injection at the site of infarct[69]. These animals were sacrificed eight weeks later (nine weeks after LAD ligation induced infarction). A third group of healthy rats (n = 2) was used as a control. The hearts were excised and fixed in 10% formalin*. The heart samples were then sectioned axially to either 0.5, 1, or 2-mm thickness for imaging (see Fig. 2.1a). The final thickness of the samples has no effect on our two-photon microscopy results, as imaging was restricted to the first ≈ 50 μm layer of tissue where signal was strongest. After two-photon imaging, histology with Masson's trichrome staining was performed for one sample of each group. Masson's trichrome stains collagen and connective tissue in blue, cytoplasm in red/pink, and nuclei in dark red/purple.

Group	Procedure	Treatment	End point
Myocardial infarction (n = 5)	LAD ligation (t= 0)	None	t = 9 weeks
Stem cell treatment (n = 4)	LAD ligation (t = 0)	Stem cell injection (t = 1 weeks)	t = 9 weeks
Healthy (control) (n = 2)	None	None	–

Table 2.1: Procedure, treatment and end point for the different animal groups used in the two-photon microscopy study.

*According to Yasui *et al.*[70] formalin fixing slightly increases SHG intensity but does not otherwise affect SHG signal.

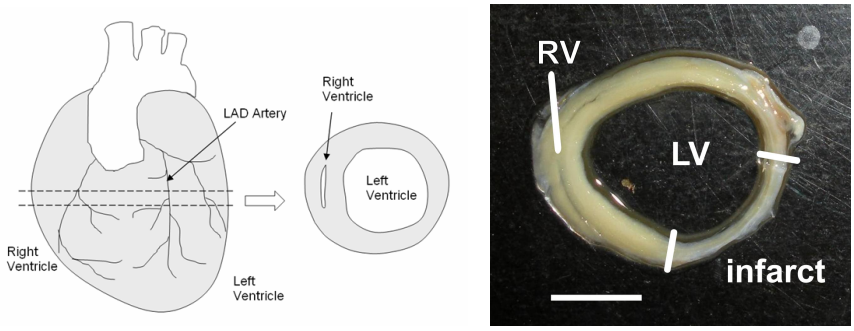

(a) (b)

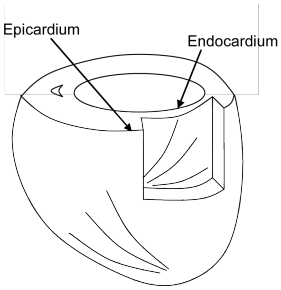

(c)

Figure 2.1: (a) Location of axial slices through the rat hearts. LAD artery: left anterior descending artery. (b) Location of infarct on one of the infarcted rat heart samples. RV, LV: right (collapsed) and left ventricles. Scale bar = 5 mm. (c) Change in fiber alignment from epicardium to endocardium.

2.3 Results

The emission spectrum in two different regions of an image is shown in Figure 2.2. The first region exhibits a sharp peak at 420 nm, which is the expected spectral signature of SHG for an excitation wavelength of 840 nm. The second region shows very little signal at 420 nm, but rather a broad spectrum from roughly 440nm to over 560 nm, consistent with the expected result of the superposition of many individual fluorophores' spectra. The fact that the 420 nm peak shifted when the excitation wavelength was changed (always centered at half the excitation wavelength) as well as its distinct, narrow shape are strong indications that the 420 nm peak represents true SHG emission. If the fluorescence contribution to the 400-430 nm signal were important, we would expect (because of the broad autofluorescence spectrum) to observe a positive correlation between the pixel intensities in this range and at higher wavelengths. However, we observed no such correlation, which suggests that the fluorescence contribution to the 400-430 nm signal is negligible. For this and all subsequent images, therefore, the SHG signal was collected at 400-430 nm (displayed in green pseudocolor) and the TPEF signal was collected at 430-460 nm (displayed in red pseudocolor).

Two sources of SHG signal have been reported in heart tissue: collagen and myosin. Type I collagen is known to produce a very strong SHG signal[41,42]. Type III collagen produces a much weaker, if any, signal[71], while non-fibrillar collagen types and other extra-cellular matrix components (elastin and fibronectin) produce no signal[41,72]. Myosin (which is present in the sarcomeres of striated muscle) also produces SHG signal[45], though this signal is weaker than that from collagen[53]. In these samples, the majority of SHG production is clearly attributable to collagen, as evident from the fibrillar and non-striated aspect of the SHG-producing features in most images. However, a few SHG-producing features (in infarct tissue) show striated patterns and could therefore arise from myosin: these are discussed in more detail below. As for the two-photon autofluorescence, many

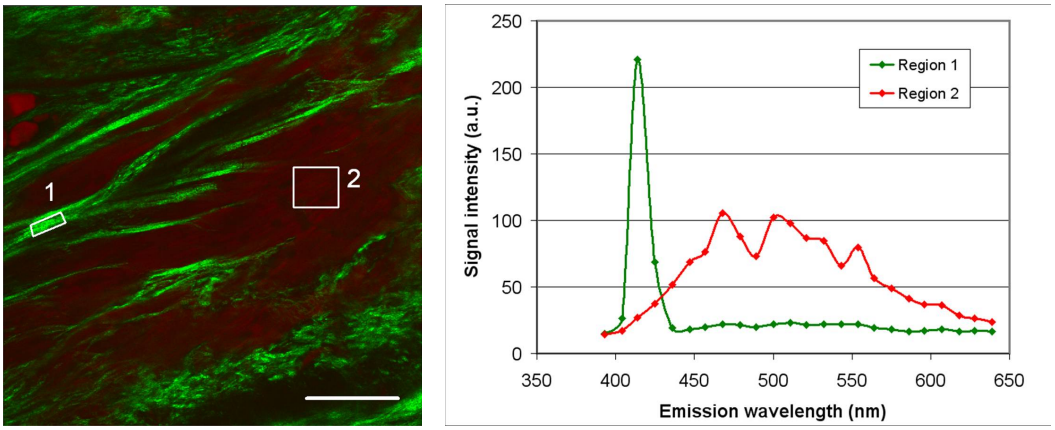

(a) (b)

Figure 2.2: Spectral decomposition of SHG and TPEF signals. (a) SHG (in green pseudocolor) is collected from 400-430 nm while TPEF (in red pseudocolor) is collected from 430-460 nm. Scale bar = 100 μm. (b) Emission spectra for the two regions selected in (a).

endogenous fluorophores, including NADH and flavins, likely contribute to the observed signal[41,44].

Figure 2.3 shows the histology and a two-photon microscopy image of healthy myocardium in the ventricular wall. There is very little collagen visible on the histology (stained blue). The two-photon images also reflect this, with only a few collagen strands visible in Fig. 2.3b. The myocytes are packed densely and reflect the double-spiral structure of the heart, i.e. fibers in the mid-wall orientated circumferentially and lying in the axial (and imaging) plane, and with fibers in the epicardium and endocardium oriented out of the axial plane (see Fig. 2.1c). This is consistent with the observations of Pope *et al.*[73], who report a similar transmural shift in the orientation of cardiomyocytes.

Figure 2.4 shows histology and two-photon images from remote and infarcted regions of LAD-ligated hearts (no treatment). (For the purpose of this work, "remote" regions were identified as any region distant by at least 1 mm of the (visually identified) scar). The histology reveals an extensive infarct and thinned ventricular walls. The infarct

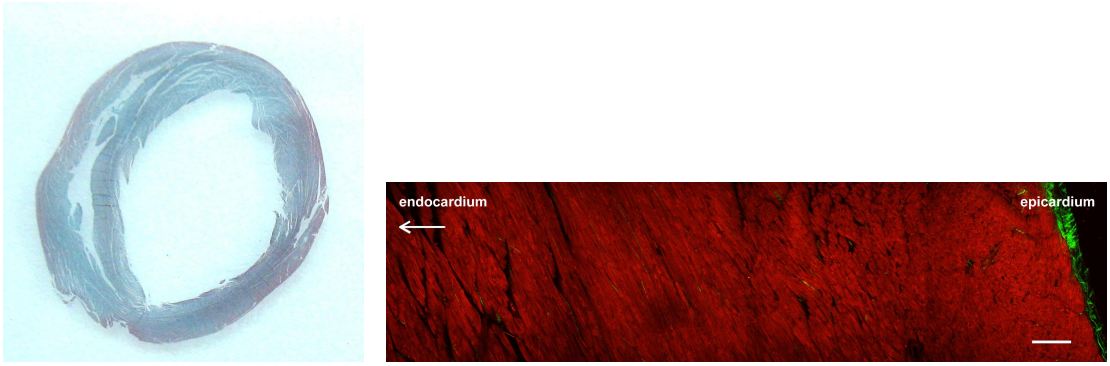

(a) (b)

Figure 2.3: Healthy myocardium. (a) Histology (Masson's trichrome stain: collagen and connective tissue in blue, cytoplasm in red/pink, and nuclei in dark red/purple). (b) Representative two-photon microscopy image of the ventricular wall. Scale bar = 100 μm.

regions showed a high degree of sample-to-sample variation: for instance, most but not all scars were transmural (i.e., spanned from the inside to the outside of the ventricular wall). This high variation was also observed on two-photon images of the infarct regions, which revealed not only sample-to-sample variation but also high heterogeneity even between different regions of a same sample. The remote regions (Fig. 2.4b) show little collagen content and reveal similar myocyte orientation as in Fig. 2.3b, implying these remote regions are relatively healthy. The infarct regions (Fig. 2.4c and 2.4d) show lower density of myocytes than in the remote region and considerably higher collagen content. In Fig. 2.4c the collagen is highly linear and runs alongside a few myocytes, while in Fig. 2.4d the collagen in much more "wavy" and there is a nearly complete absence of myocytes.

While SHG-producing features in Fig. 2.3b, 2.4b and 2.4d can be straighforwardly identified as collagen because of their district fibrillar aspect (single, elongated strands are apparent) and/or because of the absence of striation characteristic of sarcomere, a few SHG-producing features in Fig. 2.4c present a periodicity similar to that of sarcomeres. The most regular of these patterns (white arrows) have a period of between $\approx 3-7\,\mu m$,

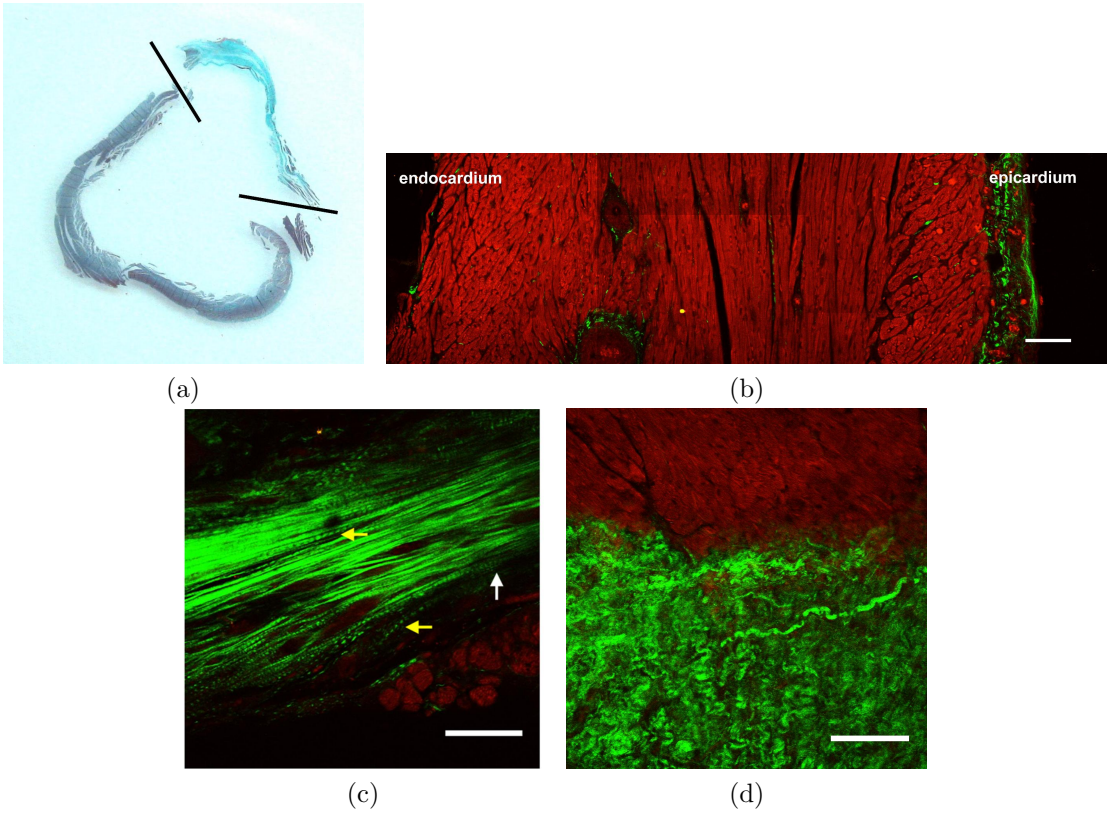

Figure 2.4: Myocardial infarction sample. (a) Histology (Masson's trichrome stain: collagen and connective tissue in blue, cytoplasm in red/pink, nuclei in dark red/purple). The infarct is located between the bars. (b) Representative two-photon microscopy image of a region away from site of infarct. (c) Image taken from the site of infarct. Most of the SHG signal is from collagen; in a few striated regions, the SHG is due to myosin from sarcomeres (white arrow = sarcomeres); thinner, longer, or irregular striated patterns are created by collagen strands (yellow arrows = striated collagen features). (d) Another representative image of a site of infarct (different animal). Scale bars = 100 μm.

which is slightly longer than the expected length of healthy sarcomeres ($\approx 2\,\mu m$[74]), and a width of $\approx 10 - 20\,\mu m$, which is consistent with myocytes. The longer-than-expected period of the pattern might be due to an oblique orientation of the myocyte in the plane, which would cause the observed sarcomere pattern to be longer than the true length of sarcomeres. These patterns were never visible in healthy or remote regions: the appearance of SHG signal from sarcomeres in infarcted but not healthy myocytes could be due to a hyperextension of the sarcomeres in infarcted tissue: hyperextension of sarcomeric pattern has been observed in disease myocytes[46], and the intensity of emitted SHG is known to be dependent on sarcomere length (Both *et al* have shown that mice sarcomeres show a four-fold increase in SHG intensity when stretched from 2 μm to 3 μm[75]).

Many other regular or quasi-regular SHG-producing structures structures visible in Fig. 2.4c (yellow arrows), however, are too thin or too irregular to be sarcomere patterns and are more likely attributable to collagen features displaying a segmented appearance (similar to features observed by others[39,50]), either because of destructive interference*, or because of a wavy pattern in the fiber causing the intensity of the SHG to dim periodically over the stretches where the alignment of the fiber is perpendicular to the incident light polarization (see Discussion).

Figure 2.5 shows histology and two-photon images of stem-cell treated rat hearts. Histology shows the extent of the scar is smaller, and the ventricular walls not as thin, as in Fig. 2.4a, implying partial tissue remodeling. Once again, on two-photon microscopy images, the remote region (Fig. 2.5b) shows densely packed myocytes with few collagen strands, while the infarct regions shows a high collagen content as well as a few striated features attributable to sarcomeres (white arrows). Fig. 2.5c shows a region of interwoven

*The SHG wave is coherent with the initial wave at its point of emission, but because the phase velocities for ω and 2ω are different, SHG waves emitted further will be out-of-phase with waves emitter earlier, resulting in constructive or destructive interference.

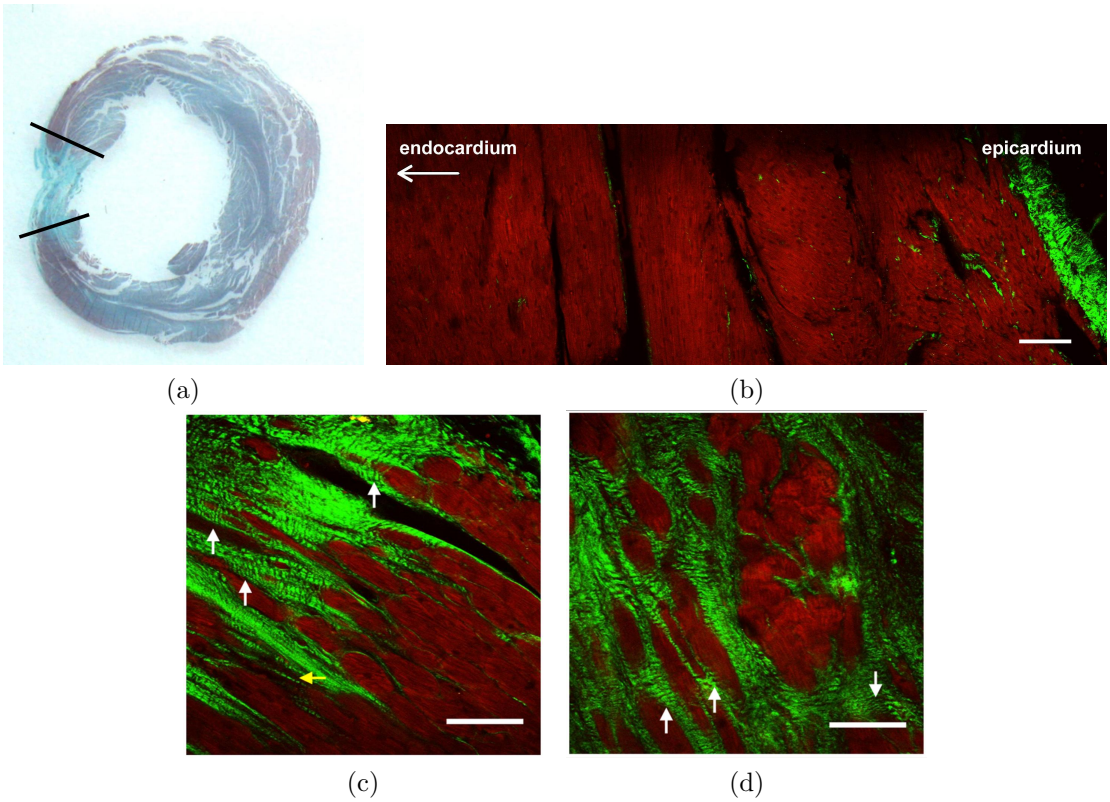

Figure 2.5: Stem-cell treated sample. (a) Histology (Masson's trichrome stain: collagen and connective tissue in blue, cytoplasm in red/pink, nuclei in dark red/purple) The infarct is located between the bars. (b) Stem-cell treated sample, region away from site of infarct. White arrows = sarcomeres; yellow arrows = striated collagen features. (c) Site of infarct in a stem-cell treated heart. (d) Another representative image of the site of infarct after cell treatment. Scale bars = 100 μm.

myocytes and collagen located near the edge of the scar, while in Fig. 2.5d the collagen forms a dense mesh around myocytes in the scar. In contrast to untreated hearts, we found a less sharp boundary between scar and healthy tissue, as well as fewer areas entirely devoid of myocytes. Quantification of these regeneration changes (in terms of collagen and myocyte content) would require imaging the entire area of the scar, which was not possible due to our limited field of view.

2.4 Discussion

2.4.1 Characterization of the second harmonic generation signal

A few remarks on the characterics of the SHG signal are warranted. Because SHG is a coherent superposition of emission contributions from individual molecules, it produces directed radiation patterns, unlike TPEF which produces an isotropic glow in all directions. SHG emitted from collagen molecules is known to be preferentially emitted in the foward direction, and the magnitude of the foward/backward anisotropy is dependent on the size of the fibrils: the largerst fibrils emit considerably more SHG signal in the forward direction while smaller fibrils ($\approx$ 40 nm diameter) show an approximately equal forward/backward distribution[42]. As our setup collects SHG signal in backscatter geometry only, we may be somewhat more sensitive to contributions from immature collagen fibrils (which are smaller) than from larger fibrils.

SHG intensity is dependent on the angle between the collagen (or myosin) fibril and the polarization of light[42]. The SHG signal is maximized when the incident light polarization and fibril are parallel, and then gradually decreases to become minimal when they are perpendicular. For instance, studies in rat tail tendon[76] have found the intensity of SHG when the incident polarization and fibrils are parallel to be roughly four times larger than the intensity of SHG when they are perpendicular. Because the Chameleon laser used for this study is linearly polarized, we observe a dependence of the intensity on the orientation of SHG-producing features. Figure 2.6 shows two-photon images of the same region under different incident polarization: the second image taken with the sample rotated by 90° with respect to the first (but is shown here in the same orientation to facilitate comparison). (Note that no polarizers were used on the emission end, so that our collected signal is independent of the polarization of the emitted SHG signal.)

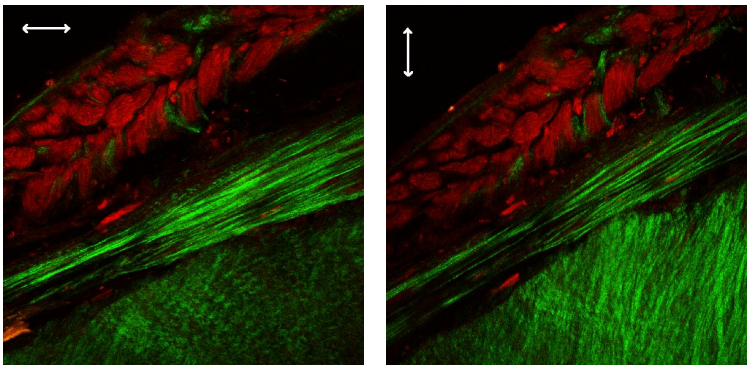

(a) (b)

Figure 2.6: Two-photon microscopy images of the same region taken with different incident polarizations (white arrows: approximate orientation of the incident light polarization). The incident polarization of the laser cannot be changed, so the sample was rotated by 90° to take the second image. The fluorescence intensity is not affected by the polarization of incident light.

Consistent with Freund *et al*[76], we find that in highly aligned fibers (e.g. middle portion of Fig. 2.6), the SHG signal undergoes a roughly four-fold change in intensity. Regions of disorganized collagen (e.g. lower portion of Fig. 2.6), however, show lower dependence on sample orientation, with modest increases in intensity (ranging from 50% to 150%) between the sample positions producing minimum and maximum SHG intensity. This is likely due to the non-uniform orientation of individual fibrils in these regions. Because the SHG intensity of collagen is quite high, we found that fibers remained visible even in the orientation producing lowest SHG intensity. Precise quantitative characterization of the SHG signal, however, would require circularly-polarized incident light to avoid these orientation-dependent intensity effects.

2.4.2 Injury and regeneration mechanisms

The two-photon microscopy results shown here are consistent with the known mechanisms of injury in infarcted myocardium, namely, the accumulation of scar tissue (collagen), tissue necrosis (decrease in viable myocytes), and adverse remodeling of tissue (thinning

of the ventricular wall and disruption in the alignment and orientation of remaining myocytes). Further, these results support the hypothesis that both limitation of collagen accumulation in the scar, and prevention of necrosis of mycoytes in the infarct region, may be potential mechanisms of functional improvement by stem-cell regeneration. This is consistent with published research that has shown that injection of mesenchymal stem cells can improve cardiac function in rats by preserving remote matrix architecture and preventing ventricular dilation[8], as decreased collagen content and necrosis would presumably reduce scar stiffness and cell slippage and help curb ventricular remodeling. Quantitative comparison of volumetric, wide field-of-view two-photon data could yield more information than histology on the organization of scar tissue, while at the same time avoiding the potential distortion of samples associated with the very thin cuts necessary for histology.

2.5 Conclusion

This work shows the use of two-photon autofluorescence and second-harmonic generation to image endogenously and simultaneously both the myocytes and the collagen components of chronically infarcted and stem-cell regenerated heart. These results provide insight into the structural changes undergone after injury and treatment: namely, that that remote myocardium remains similar to healthy myocardium in structure and composition; that infarcted myocardium has high contents of collagen which can be linear or disorganized, and areas with very little or no myocyte content; and that stem-cell treated infarcted myocardium shows more myocytes intertwined with collagen strands. Adequate quantification of changes in composition and structure (collagen area/volume, myocyte transmural orientation, collagen organization/disarray) will require a larger field of view (ideally, whole-slide imaging) and volumetric data acquisition, but could provide

interesting information about the mechanisms of stem-cell cardiac regeneration.

Chapter 3

Polarimetry

3.1 Theory

As mentioned in Section 1.3, interesting properties can be revealed by probing tissues with polarized light. Loss of polarization (depolarization), rotation of the polarization state (retardance) and differential attenuation of polarization states all reflect medium properties. Because all these effects occur simultaneously, however, the output polarization states reflect the combined effect of many different processes and interpreting these results is therefore challenging.

Many different strategies have been used to interpret results from polarimetry. Some groups have looked directly at the elements of the output Stokes vector[77,78], $\mathbf{S_o} = (I\ Q\ U\ V)^T$, where I represents the overall intensity of the beam, Q gives the intensity of linear polarization along horizontal and vertical axes, U gives the intensity of linear polarization at $\pm 45°$, and V gives the intensity of light that is (right- and left-) circularly polarized. Others have used elements of the Mueller matrix of a sample[79], which is a four-by-four matrix representing the transfer function of the polarization state of light (and which relates the input and output polarization states via $\mathbf{S_o} = \mathbf{M}\ \mathbf{S_i}$) or

a ratio of the perpendicular and parallel components of polarized light called the polarization ratio[56,57]. There are also ways of extracting individual parameters from the Mueller matrix. For instance, Pravdin *et al.*[80] have proposed rotational invariants of Mueller matrices as a way of characterizing tissue. The Mueller matrix can also be decomposed to yield values for individual optical parameters[61], including a depolarization index[81], degree of polarization[59], or birefringence/linear retardance[82,83]. Our group has used Mueller matrix decomposition to extract values of various parameters: this has been shown to produce good estimates of the known properties of optical phantoms and in Monte Carlo simulations[36].

As mentioned in Section 1.3, birefringence is the measure of a difference in the refractive indices for polarizations parallel (n_e) and perpendicular (n_o) to the extraordinary* axis : $\Delta n = n_e - n_o$. However, Eq. 1.1 which was stated earlier and relates linear retardance and birefringence, is somewhat simplified. The more accurate version of this equation relates the linear retardance to the *apparent* birefringence, Δn_{app}:

$$\delta_{app} = \frac{2\pi}{\lambda} \cdot d \cdot \Delta n_{app} \tag{3.1}$$

where we now write δ_{app} to emphasize this. The *apparent* birefringence, contrary to Δn, is dependent on the angle between a material's anisotropy axis (orientation of the optical axis) and the beam interrogating the sample[84]. This dependence can be expressed as a function of the elevation angle φ (the angle between the anisotropy axis and the imaging plane, i.e., the plane perpendicular to the probing beam) (see Fig. 3.1):

$$\Delta n_{app} = n(\varphi) - n_o \tag{3.2}$$

*The extraordinary axis is also often referred to as the optical axis. It corresponds to the anisotropy axis of a material: "optical axis" and "anisotropy axis" are therefore used interchangeably here.

where $n(\varphi)$, the apparent index of refraction, is found as follows:

$$\frac{1}{n^2} = \frac{\cos^2\varphi}{n_e^2} + \frac{\sin^2\varphi}{n_o^2} \tag{3.3}$$

We can rewrite the linear retardance to make its dependence on φ more explicit as follows:

$$\delta_{app} = \frac{2\pi}{\lambda} \cdot d \cdot \Delta n \cdot \frac{\left[\left(\frac{n_e}{n_o}\right)^2 \cos^2\varphi + \sin^2\varphi\right]^{-1/2} - 1}{\frac{n_e}{n_o} - 1} \tag{3.4}$$

Thus, the apparent value of linear retardance δ_{app} will be maximal (and reflect "true" sample birefringence) when the light is propagated perpendicular to the anisotropy axis, i.e. $\varphi = 0°$ (see Fig. 3.1), and will be null when the light propagates along the anisotropy axis, i.e. $\varphi = 90°$. The measured (apparent) linear retardance through a sample is therefore a function of both the sample's anisotropy and its geometric orientation with respect to the probing beam.

Despite this ambiguity in the interpretation of the linear retardance values, polarimetry was used here to compare two different models of myocardial infarction* The ambiguity in the interpretation of the linear retardance values will be discussed more thoroughly in Chapter 4.

3.2 Methods

3.2.1 Polarimetry experimental setup

Figure 3.2 shows a schematic of the experimental polarimetry setup. It determines the transfer function of light polarization as it interacts with a sample (by measuring the output polarization for different input polarization states) in the form of the four-by-

*Some of the data presented here is included in a paper (to be submitted) comparing these two infarction models (see Wu *et al.*, 2010[85]).

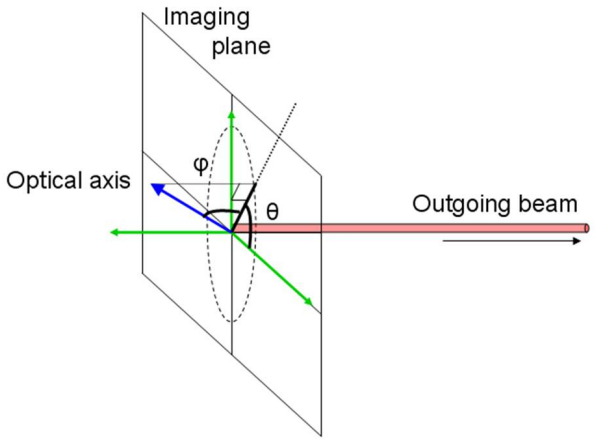

Figure 3.1: Angle definitions: the elevation angle φ is the angle between the anisotropy (optical) axis and the imaging plane, i.e., the plane perpendicular to the probing beam; the azimuthal angle θ is angle between a reference axis and the projection of the anisotropy axis onto the imaging plane.

four Mueller matrix. To obtain the output Stokes parameters corresponding to all input states, light from a 635 nm diode laser (ThorLabs) was polarized either linearly or circularly by a combination of a linear polarizer and a removable quarter-wave plate. Samples were illuminated off-axis by $\chi = 20°$ (see Fig. 3.2) in order to prevent direct laser light saturating the detector. Upon the light exiting the sample, one polarization state at a time (linear or circular) was selected using a second combination of a removable quarter-wave plate and a linear polarizer (polarization analyzer). The light was finally recorded by a CCD camera (Photometrics CoolSnap K4). Note that while systems with dynamic polarization modulation and synchronous detection have been used previously to increase signal-to-noise ratio on single-point measurements (by using a photoelastic modulator to modulate the light polarization at a known frequency)[36], this was not deemed necessary for this imaging study.

Four input states (horizontal, vertical, +45°, right-circularly polarized) and six output states (horizontal, vertical, ±45°, right- and left-circularly polarized light) were recorded, for a total of twenty-four combinations per sample. The output Stokes parameters for

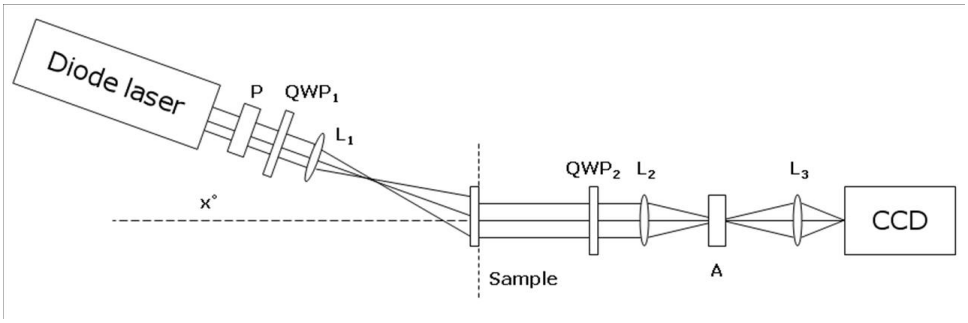

Figure 3.2: Experimental polarimetry setup. P: polarizer, QWP_i: quarter-wave plate, L_i: lens, A: analyzer.

each of the four input states were measured from the detected intensities with each of the six output configurations in the following way:

$$\begin{aligned} I &= I_{180^\circ} + I_{90^\circ} \\ Q &= I_{180^\circ} - I_{90^\circ} \\ U &= I_{45^\circ} - I_{135^\circ} \\ V &= I_R – I_L \end{aligned} \tag{3.5}$$

where the subscripts indicate the output state being detected. The output Stokes vectors correspond to each input state were then used to calculate the elements of the Mueller matrix as follows:

$$\mathbf{M}(i,j) = \begin{bmatrix} \frac{1}{2}(I_H + I_V) & \frac{1}{2}(I_H - I_V) & I_P - \mathbf{M}(1,1) & I_R - \mathbf{M}(1,1) \\ \frac{1}{2}(Q_H + Q_V) & \frac{1}{2}(Q_H - Q_V) & Q_P - \mathbf{M}(2,1) & Q_R - \mathbf{M}(2,1) \\ \frac{1}{2}(U_H + U_V) & \frac{1}{2}(U_H - U_V) & U_P - \mathbf{M}(3,1) & U_R - \mathbf{M}(3,1) \\ \frac{1}{2}(V_H + V_V) & \frac{1}{2}(V_H - V_V) & V_P - \mathbf{M}(4,1) & V_R - \mathbf{M}(4,1) \end{bmatrix} \tag{3.6}$$

where the indices i and j respectively denote the rows and columns of the Mueller matrix, and where the subscript corresponds to the input polarization state (V: vertical,

H: horizontal, P: +45°, R: right-circular) (e.g. Q_V is the horizontal component of the output light for input light that is vertically polarized).

This resulting Mueller matrix reflects the lumped effects of simultaneously occurring complex processes such as depolarization, diattenuation, and retardance[61,86]. In order to extract and quantify individual polarization effects, Mueller matrix decomposition (see section 3.2.2) is performed, circumventing the difficult problem of interpreting the Mueller matrix elements.

3.2.2 Mueller matrix decomposition

Mueller matrix decomposition was performed at each pixel to obtain the linear retardance δ and the azimuthal angle θ (see Fig. 3.1). A thorough description of the Mueller matrix decomposition developed by our group (Mike Wood, Nirmalya Ghosh) has been published elsewhere[62], so only a brief review of the relevant sections will be provided here.

The full Mueller matrix $\mathbf{M}$ can be decomposed into three constituent matrices representing the effects of individual polarization processes as follows

$$\mathbf{M} = \mathbf{M_\Delta M_R M_D} \tag{3.7}$$

where the effects of depolarization are described by the depolarizing matrix $\mathbf{M_\Delta}$, the effects of linear birefringence and optical activity (circular birefringence) are described by the retarder matrix $\mathbf{M_R}$, and the effects of linear and circular dichroism are described in the diattenutor matrix $\mathbf{M_D}$[62,87]. Note that while matrix multiplication is non-commutative (so that there are other possible orders of the constituent matrices in Eq. 3.7), for samples with low diattenuation (including biological tissues of interest), it

can be shown that the multiplication order has very little influence on the final value of the extracted parameters[88].

The linear retardance (δ) can be calculated from the elements of the retarder matrix $\mathbf{M_R}$ as[61]

$$\delta = \cos^{-1}\left(\sqrt{\left(m_R(2,2) + m_R(3,3)\right)^2 + \left(m_R(3,2) - m_R(2,3)\right)^2} - 1\right) \tag{3.8}$$

where $m_R(i,j)$ are the elements of $\mathbf{M_R}$. In order to find the azimuthal angle, the retarder matrix must be further decomposed into two matrices representing the effects of linear retardance and chirality: $\mathbf{M_R} = \mathbf{M_{LR}}\mathbf{M}_\psi$. The linear retardance matrix $\mathbf{M_{LR}}$ is therefore found by $\mathbf{M_{LR}} = \mathbf{M_R}{\mathbf{M}_\psi}^{-1}$, where $\mathbf{M}_\psi$ is the matrix associated with the circular retardance (optical activity). The azimuthal angle θ can finally be calculated from the elements of $\mathbf{M_{LR}}$ as

$$\theta = 0.5\ tan^{-1}\left(\frac{m_{LR}(2,3) - m_{LR}(3,2)}{m_{LR}(3,1) - m_{LR}(1,3)}\right) \tag{3.9}$$

If the light propagation distance in the sample d is known, the measured retardance δ can be used to calculate the sample birefringence (via Eq. 3.1). This is not necessary though, as direct comparisons can be made between values of linear retardance for different samples as long as the pathlength is constant. If we assume the optical properties (e.g. scattering coefficient) of the samples are roughly constant, we can consider that the pathlengths through equal thickness of tissue will be the same. As the composition of healthy and infarcted tissues are different, it might be expected that their optical properties would differ slightly; however, we find that the polarization retention of light through infarcted and healthy portions of the myocardium is roughly constant, which suggests

that the scattering coefficient (and therefore, the optical pathlength) does not vary much.

3.2.3 Phase wrap-around correction

Because retardance is a phase shift that accrues between two orthogonal polarization states, it reaches a maximum value after which the retardance starts to decrease. For this reason, a phase wrap-around artefact appears when the phase shift reaches and exceeds a value of 180°: as this happens, the measured linear retardance value will peak and then decrease until no linear retardance is measured at all (when the real phase shift is 360°) (Fig. 3.3). Thus, the maximal value that we can measure unambiguously is 180° degrees.

Extracted values of azimuthal orientation (θ) also suffer from an artefact when the phase shift exceeds 180° which make the values of θ discontinuous, unlike the linear retardance values. Each multiple of 180° in phase shift introduces a sign error in $\mathbf{M_{LR}}$ that changes the value of θ by 90° (Fig. 3.3).

When imaging samples, this discontinuous θ-orientation effect can be exploited in order to significantly reduce the ambiguity due to phase wrap-around. Changes in $\theta-$orientation of 90° over a distance of a single pixel are highly unphysical, and therefore can be used as markers of phase wrap-around artifact which we can take advantage of to "unwrap" the phase. Adjacent pixels presenting values of linear retardance near 180° or 0° and values of θ separated by exactly 90° are observed at the border of a region of wrapped-around pixels. This provides a way of finding the "border" surrounding regions of wrap-around, but it remains to be determined which side of the "border" is wrapped-around. This can be resolved by our expectation that linear retardance should drop at the very edges of the sample (where certain photons have decreased pathlength,

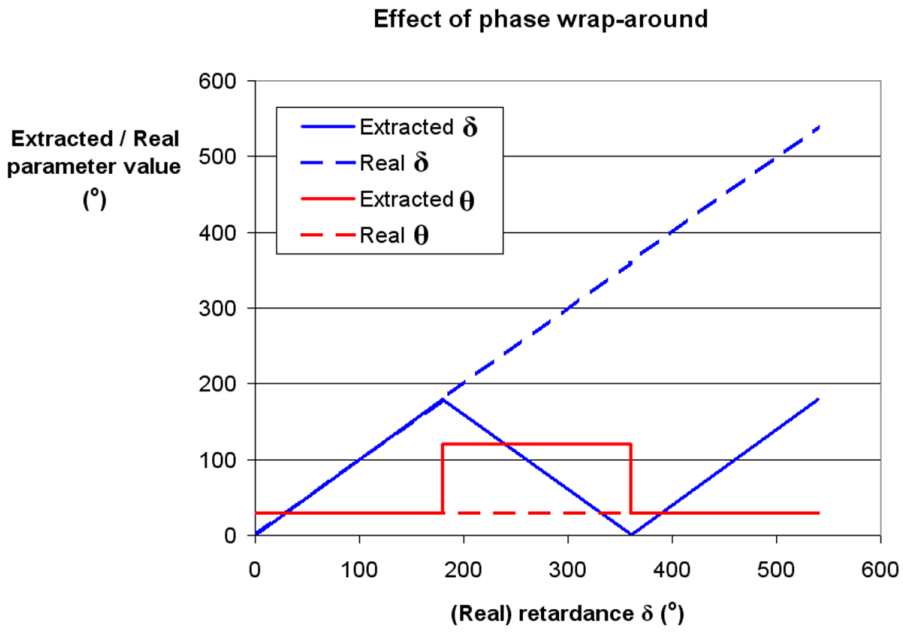

Figure 3.3: Effect of wrap-around artifact on extracted linear retardance δ and orientation θ values (as obtained from Mueller matrix decomposition), as a function of increasing real linear retardance, for a material with (real) orientation $\theta = 30°$.

resulting in lower retardance values). In this way, the measureable range of δ values can be extended to $0° - 360°$.

3.2.4 Rat models of myocardial infarction

All animal studies were performed at the Toronto General Hospital and carried out under institutional approval from the University Health Network, under the lead of Dr. Ren-Ke Li's group. The results shown here are of cardiac samples from two different Lewis rat models of myocardial infarction[85]. The first group of rats (myocardial infarction, MI, n=4) underwent permanent left anterior descending (LAD) coronary artery ligation and the animals were sacrificed nine weeks post ligation (see Table 3.1) (same samples as "untreated" group in Chapter 2). Animals in the second group (ischemia/reperfusion, IR, n = 6) underwent a 60-minute ligation of the LAD artery, followed by reperfusion, and were also sacrificed nine weeks post ligation. The third group of rats (control, n =

3) underwent a sham ligation and were sacrificed nine weeks later. All the hearts were excised, fixed in 10% formalin, and sectioned axially to 0.5-mm thickness (see Fig. 2.1a) for polarimetry imaging.

Group	Procedure	End point
Myocardial infarction (MI) (n = 4)	permanent LAD ligation (t= 0)	t = 9 weeks
Ischemia/Reperfusion (IR) (n = 6)	60-minute LAD ligation (t = 0)	t = 9 weeks
Sham-operated (control) (n = 3)	None	t = 9 weeks

Table 3.1: Procedure and end-point for each animal group used in the polarimetry imaging study.

3.3 Results

Figures 3.4 - 3.6 show typical images of hearts from the sham and infarcted groups. The sham-operated hearts (Fig. 3.4) present a low-high-low pattern from the inner to the outer ventricular wall. The linear retardance values are roughly constant around the ring, with the right ventricle often showing slightly lower linear retardance than the left ventricle. Notice also the nearly constant ventricular wall width for this sample.

The hearts from the MI group (permanent ligation) (Fig. 3.5) no longer exhibit constant linear retardance values in the infarct region, with values almost always lower than in the remote regions (with the exception of a few high-retardance patches). The low-high-low pattern that is observed in healthy hearts and in regions remote from the site of infarct is also disrupted in the infarct region. Finally, the ventricular wall thickness

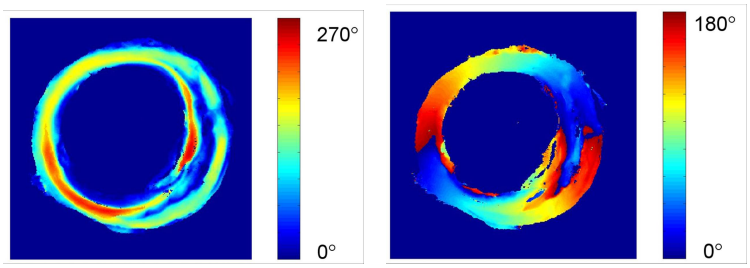

(a) (b)

Figure 3.4: Polarimetry imaging of a sham-operated rat heart. (a) Linear retardance (°) (b) Azimuthal angle of anisotropy axis θ (°).

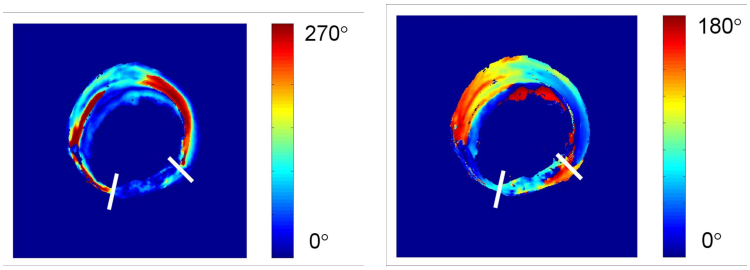

(a) (b)

Figure 3.5: Polarimetry imaging of a myocardial infarction model (permanent ligation) rat heart. (a) Linear retardance (°) (b) Azimuthal angle of anisotropy axis θ (°). Infarct is located between white bars.

often decreases at the site of infarct.

Finally, the hearts from the IR group (60-minute ligation) (Fig. 3.6) also show generally lower linear retardance values and disrupted low-high-low pattern in the region of infarct, but these changes are less pronounced than those in the MI hearts.

The average linear retardance in the infarct and remote (supposedly healthy) regions was found for each sample. The infarct region was identified by visual inspection of the sample according to the following visual cues: thinning of the sample and whitening due to collagen accumulation. The infarct was assumed to include the entire thickness of the ventricular wall, and usually spanned $\frac{1}{8}$ to $\frac{1}{4}$ of the circumference of the heart. A margin of roughly 1 mm was left of each side of the infarct, and all other pixels were considered

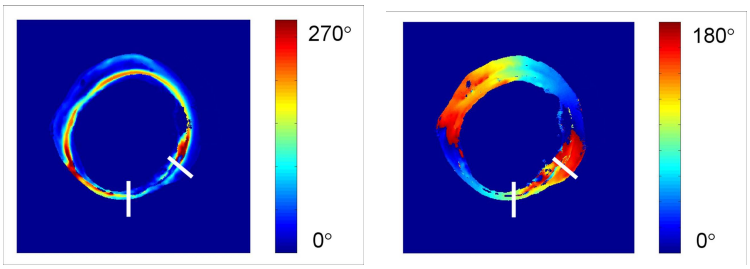

(a) (b)

Figure 3.6: Polarimetry imaging of an ischemia-reperfusion model (temporary ligation) rat heart. (a) Linear retardance (°) (b) Azimuthal angle θ (°). Infarct is located between white bars.

to be part of the remote region. The average of the pixels corresponding to each region (remote or infarct) was found for each sample; for the sham-operated hearts, the average value of all pixels was taken. The mean values for each group and region (as averaged over n=3, n=4 or n=6) are presented in Table 3.2 and Fig. 3.7. Note that based on some preliminary experiments with fresh and formalin-fixed tissues, we expect that the process of formalin fixing increases the depolarization of samples but does not significantly affect the linear retardance of our samples.

Table 3.2: Mean linear retardance for myocardial infarct (MI), ischemia/reperfusion (IR) and sham groups (error bars: standard deviation).

Group	Remote	Infarct	Ratio
MI	96 ± 14	74 ± 21	0.80 ± 0.33
IR	78 ± 18	88 ± 29	1.15 ± 0.32
Sham	92 ± 38	-	-

We find that the remote regions of the MI samples shows retardance values close to those of the sham-operated samples, while the infarct regions have lower retardance values than the remote regions (ratio = 0.80 ± 0.33). These values, while not statistically significant (p = 0.14, calculated using a two-tailed Student's t-test), show a trend consistent with previously published results showing decrease linear retardance in the infarct region[36,60], though the reduction measured here (roughly 20%) was not as large as

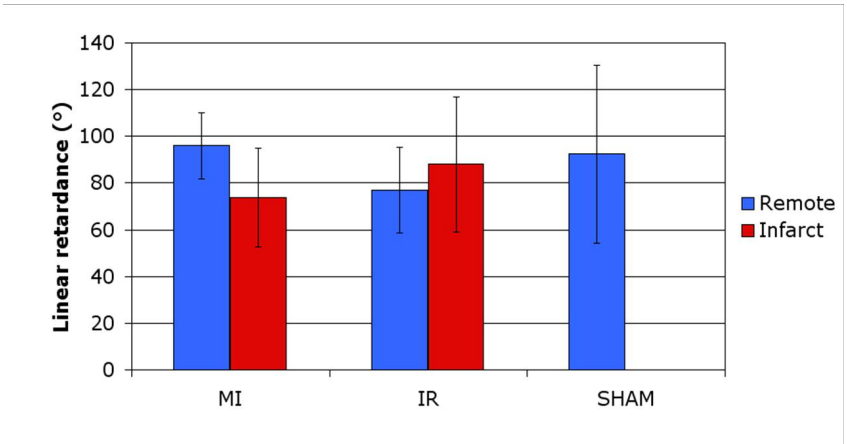

Figure 3.7: Mean ± standard deviation of linear retardance (°) for myocardial infarct (MI), ischemia/reperfusion (IR) and sham groups.

that described earlier (70-86%). Different measurement methods (imaging versus point measurements, no wrap-around correction, different sample thickness) may account for this discrepancy. On the other hand, the linear retardance values of IR samples for both remote and infarct regions are higher than those for MI and, interestingly, are somewhat higher in the infarct region than in the remote region (ratio = 1.15 ± 0.32, p = 0.45). This suggests that the two models create different injuries, with ischemia/reperfusion (IR) resulting in a less severe and more diffuse injury than the permanent ligation (MI). Note that neither of these differences (infact versus remote linear retardance, for MI and for IR model) achieved statistical significance. This is largely due to a large sample-to-sample variation in absolute values of linear retardance, as attested by the large standard deviation values. Figure 3.8 shows intersample variation for the three samples in the sham-operated group: the average value of linear retardance for the first sample is more than double that for the last sample. These differences might be due to inconsistencies in sample processing either during sample collection, or after formalin fixing (e.g. imperfect axial cut, damage to the sample from handling, etc.). These samples are also highly heterogenous, so that while in general the infarct has lower retardance values, some samples contain small areas (few pixels) that have quite high retardance, which results in a high standard deviation and an average that is skewed towards high linear retardance values.

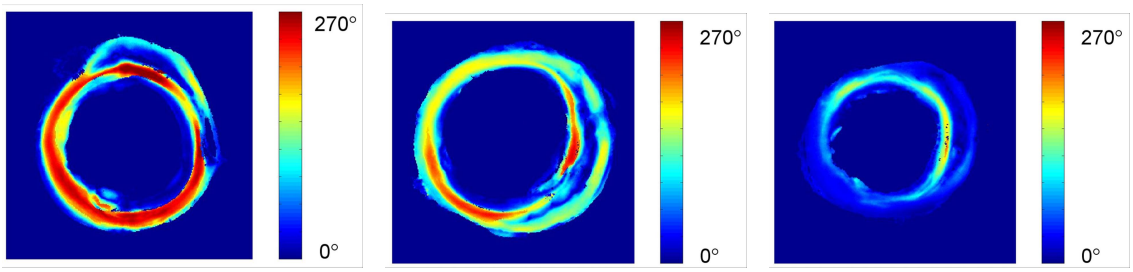

(a) (b) (c)

Figure 3.8: Linear retardance images for the three samples in the sham-operated group (identical procedure for all three samples), showing puzzlingly large variation in linear retardance value from one sample to the next.

3.4 Comparison to two-photon microscopy

We compared these polarimetry images with two-photon microscopy images of the same samples to gain insight into the underlying cause for the observed changes in linear retardance following injury. It had been hypothesized that the observed changes mostly reflected alterations in the extracellular matrix, as collagen is known to be highly birefringent: it was expected that collagen in scar issue would be more disorganized than that in the healthy tissue, making the tissue more isotropic and lowering its birefringence. In order to evaluate this, we performed two-photon microscopy of samples from the MI, IR and sham groups and compared side-by-side two-photon images with the corresponding regions on polarimetry images. The registration between images from each modality was not perfect as we had no common coordinate system: registration was done approximately and by eye, which became quite difficult when the features were small and the tissues highly heterogenous (as was often the case in the infarct region). Note also that the volumes sampled by each modality are different: polarimetry results represent the integrated optical properties over the whole thickness (0.5 mm) of the sample, while the two-photon results show a depth-sectioned slice through the tissue. Nevertheless,

comparison of approximately corresponding areas/features in the two-photon and polarimetry images did prove insightful.

Comparison of the linear retardance and two-photon microscopy images reveals that two distinct effects account for the variation of linear retardance across the tissue. Firstly, we find that the linear retardance values reflect the composition of the tissue (collagen and myocytes). Myocytes are an important contributor to linear retardance, as healthy regions displaying very little collagen nevertheless exhibit high linear retardance. Linear collagen regions (such as the one seen in Fig. 2.4c of the previous chapter) also exhibit high retardance, as expected, but wavy collagen regions (such as the one in Fig. 2.4d of the previous chapter) show low retardance, presumably because of the disarray of the fibers, which results in a lower anisotropy.

Secondly, variations of linear retardance values in regions of uniform tissue composition (as determined on two-photon microscopy images) (e.g. regions composed almost exclusively of myocytes) reflect tissue orientation properties. Specifically, in regions of high anisotropy (i.e. regions containing either linear collagen or dense myocytes), the orientation of the anisotropy axis (i.e. the alignment of myocytes or collagen strands) with respect to the probing beam is reflected in the measured linear retardance values. This effect explains the low-high-low pattern of linear retardance observed in the healthy ventricular wall. This is consistent with expectations that the measured linear retardance should be maximal when the anisotropy axis is perpendicular to the probing beam (i.e. in the plane of imaging) and significantly lower as they become more aligned (see Eq. 3.1 and 3.3).

These results indicate that the reduced linear retardance values in regions of infarct have an ambiguous origin, as they could be due not only to a composition change (e.g.

replacement of aligned myocytes with wavy collagen), but also to a change of orientation of the myocytes (e.g. from mostly perpendicular to mostly parallel with the probing beam), which would have a similar effect on the apparent linear retardance values. A method to address this ambiguity will be presented in Chapter 4.

3.5 Conclusion

Polarimetry images have found a decrease in mean linear retardance values in the region of infarct for a permanent ligation model of myocardial infarction, and a decrease over the entire sample for a temporary ligation model. These results suggest the injuries caused by each mode of ligation were different, with the injury being less severe but more diffuse if perfusion to the ischemic muscle was restored. Furthermore, comparison of two-photon microscopy images and polarimetry data reveals that both i) tissue composition (myocytes versus collagen) and organization (linear versus wavy collagen), and ii) orientation of birefringent structures (myocytes, linear collagen), affect the apparent linear retardance. In order to separate out these two effects, the first a reflection of tissue anisotropy and the second a reflection of experimental geometry, we have developed a method that will be presented in the next chapter.

Chapter 4

Dual projection reconstruction

4.1 Concept and theory

Linear retardance can be used as an indicator of tissue anistropy, as was discussed in Section 1.3. However, as seen in Eqs. 3.1 to 3.3, linear retardance is proportional not to the true, intrinsic birefringence (which reflects tissue anisotropy), but rather to the *apparent* birefringence, Δn_{app}, which is a function of the relative orientations of the beam path and the anisotropy axis of the tissue. Thus, the apparent (measured) linear retardance is geometry-dependent. The dependence of the apparent linear retardance δ_{app} on the elevation angle φ (see Fig. 3.1) can be expressed as follows

$$\begin{aligned} \delta_{app} &= \tfrac{2\pi}{\lambda} \cdot d \cdot \Delta n_{app} \\ &= \tfrac{2\pi}{\lambda} \cdot d \cdot \Delta n \cdot F(\tfrac{n_e}{n_o}, \varphi) \end{aligned} \tag{4.1}$$

where we have expressed Δn_{app} as the product of the real birefringence Δn times the function $F(\frac{n_e}{n_o}, \varphi)$, defined as follows:

$$\begin{aligned} F(\tfrac{n_e}{n_o}, \varphi) &\equiv \Delta n_{app}/\Delta n \\ &= \frac{\left[\left(\frac{n_o}{n_e}\right)^2 \cos^2\varphi + \sin^2\varphi\right]^{-1/2} - 1}{\frac{n_e}{n_o} - 1} \end{aligned} \tag{4.2}$$

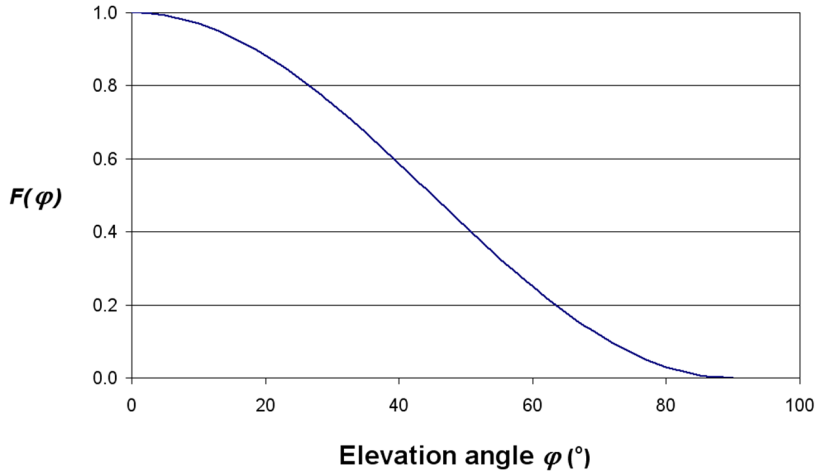

Figure 4.1: Ratio of apparent to real birefringence as a function of the elevation angle ($F(\varphi)$) for $n_e/n_o = 1.001$

which represent the ratio between the apparent and real birefringence. F is a very slowly varying function of n_e/n_o (for instance, variations of Δn over seven orders of magnitude [1×10^{-3} to 1×10^{-10}] yield changes of less than 0.001 in the value of F for any given angle) so we can effectively consider F as a function of φ only, given a reasonable estimate of the index of refraction and birefringence. Figure 4.1 shows the value of $F(\varphi)$ for $n_e/n_o = 1.001$, a value corresponding to reasonable estimate of the properties of muscle tissue, i.e. an index of refraction $n_o = 1.4$ and a birefringence $\Delta n = 1.4 \times 10^{-3}$ (Schoenenberger *et al.* report $n_o = 1.36$ and $\Delta n = 6.6 \times 10^{-4}$ for porcine myocardium[89]). From Eqs. 4.1 and 4.2, the linear retardance will be maximal when light propagates perpendicular to the anisotropy axis ($\varphi = 0°$), and will be null when light propagates along the anisotropy axis ($\varphi = 90°$) (see Fig. 4.1).

Because of the geometry-dependence of the apparent birefringence, different retardance values would be measured for a given birefringent, uniaxial material when observed from different orientations. The effects of experimental geometry therefore interfere with the interpretation of the linear retardance as a direct indicator of a material's true anisotropy. Assessing anisotropy independently of experimental geometry would

require a metric that is dependent on the true, rather than the apparent, birefringence (Δn rather than Δn_{app}), i.e., a metric that is a function of n_e and n_o but not of φ.

If the angle φ in Eq. 4.1 is known, it becomes possible to decouple the effect of experimental geometry from that of anisotropy, and thus to obtain a measure of true anisotropy that is independent of geometry. By determining two values of the azimuthal angle θ (the projection of the anisotropy axis in the imaging plane) corresponding to different incident beam directions (θ_A and θ_B), as well as two values of apparent linear retardance (δ_A and δ_B), enough information is provided to reconstruct the (three-dimensional) orientation of the anisotropy axis*. This process is analogous to finding the orientation and magnitude of a vector by from the length and orientation of its projection onto two different planes, except that the relationship between the "vector magnitude" (birefringence) and the length of the "projection" (apparent birefringence) is described by Eq. 4.2 rather than a cosine function. The details of the reconstruction algorithm are provided in Section 4.2.3.

Once the three-dimensional orientation of the anisotropy axis is known, φ can be found easily and can be substituted in $F = F(\varphi)$. Because d in Eq. 4.1 is not known, we cannot explicitly find Δn; instead, we will introduce the "reconstructed" linear retardance δ':

$$\delta' = \frac{\delta_{app}}{F(\varphi)} = \frac{2\pi}{\lambda} \cdot d \cdot \Delta n \tag{4.3}$$

as a value corresponding to the linear retardance which *would be measured* through a material of equivalent pathlength and birefringence *if the anisotropy axis were perpendicular to the probing light beam.* This metric satisfies our requirement of being dependent on

*Note that Ugryumova *et al.* report using a similar approach for polarization-sensitive optical coherence tomography, in which they take measurements of apparent birefringence for multiple incident beam angles, and reconstruct the real birefringence and anisotropy axis from these multiple values of Δn_{app} [65].

the real (Δn) rather than apparent (Δn_{app}) birefringence.

To test this dual-projection reconstruction method, we have used a birefringent polystyrene sphere of known anisotropy axis*. This has allowed us to evaluate the performance of the reconstruction method as a function of the orientation of the anisotropy axis.

4.2 Methods

4.2.1 Polystyrene sphere

The 8-mm-diameter polystyrene sphere used here was cut from a polystyrene cylinder, which is known to be birefrigent as a result of the injection moulding process. Dual-projection reconstructions were performed for various orientations of the sphere. The anisotropy axis was taken to be along the axis of the original cylinder, and was visually confirmed with crossed polarizers.

4.2.2 Polarimetry setup

The experimental setup and Mueller matrix decomposition described in Sections 3.2.1 and 3.2.2 were used (see Fig. 4.2). The only change in the experimental setup is the addition of an iris placed immediately before the sphere (not shown in Fig. 4.2) which restricted the incident light to a ≈ 1 mm spot at the very center of the sphere. Experiments were performed with the incident beam both in direct transmission (on-axis, $\chi = 0°$ in Fig. 4.2), and slightly angled (off-axis, $\chi = 8°$). When imaging biological samples of irregular shape, the latter configuration prevents the CCD from being saturated with light directly transmitted around the sample edges; we wanted to assess whether this

*The results presented here are largely the same as those in Wallenburg *et al.*[90]

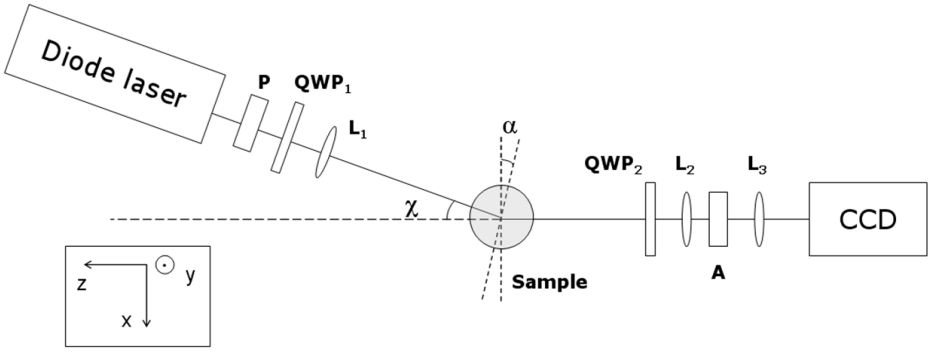

Figure 4.2: Schematic of the polarimetry imaging system used for the dual projection reconstruction. P: polarizer, QWP_i: quarter-wave plate, L_i: lens, A: analyzer. The incident beam is either on axis or off-axis by angle χ.

would introduce an error in the reconstruction. To evaluate the effect of anisotropy axis orientation on the dual-projection method, reconstructions were performed with different orientations of the sphere's anisotropy axis.

For each orientation of the sphere's axis, imaging was done twice: once with the sphere in its original position, then with the sphere rotated by an angle $15° \leq \alpha \leq 35°$ about the y-axis (see Fig. 4.2). Mueller matrix decomposition was performed at each pixel to find values of δ_{app} and θ (see Fig. 4.3), which were then averaged over all pixels in the image of the sphere to obtain a single value of δ_{app} and θ for each sphere position (i.e. δ_A, δ_B, θ_A, and θ_B). Note that the size of the sphere was chosen so that values of linear retardance were never wrapped-around (see Section 3.2.3).

4.2.3 Dual projection reconstruction algorithm

The known behavior of the apparent linear retardance (Eq. 4.1) was used to find the single anisotropy axis and reconstructed linear retardance which offered a best fit to both sets of measurements (δ_A, δ_B, θ_A, and θ_B). If $\delta' \equiv \frac{2\pi}{\lambda} \cdot d \cdot \Delta n$ is the "true" linear retardance, $\mathbf{u}$ is the unitary vector which gives the direction of the anisotropy axis at

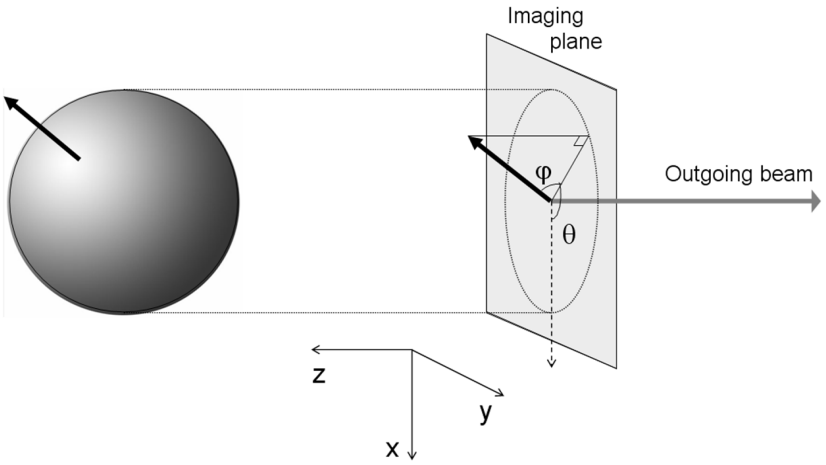

Figure 4.3: Relative geometry of the sphere anisotropy axis (dark arrow) and the probing beam (only the outgoing beam is shown here for clarity). The elevation angle φ is the angle between the anisotropy axis and the imaging (xy) plane; the azimuthal angle θ is the orientation of the projection of the sphere anisotropy axis on the imaging plane.

position A*, and $\mathbf{u}'$ is the unitary vector which gives the direction of the anisotropy axis at position B, the system of equations we need to solve is the following:

$$\begin{aligned} \delta_A &= \delta' \cdot F(\arctan \tfrac{u_z}{\sqrt{u_x^2+u_y^2}}) \\ \theta_A &= \arctan(\tfrac{u_y}{u_x}) \\ \delta_B &= \delta' \cdot F(\arctan \tfrac{u'_z}{\sqrt{u'^2_x+u'^2_y}}) \\ \theta_B &= \arctan(\tfrac{u'_y}{u'_x}) \end{aligned} \tag{4.4}$$

Using the known relationship between $\mathbf{u}$ and $\mathbf{u}'$ ($\mathbf{u}'$ is simply $\mathbf{u}$ rotated by an angle α around the y-axis) and $\delta_x = \delta' \cdot u_x$, $\delta_y = \delta' \cdot u_y$ and $\delta_z = \delta' \cdot u_z$, we we find that we have only three unknowns : δ_x, δ_y and δ_z.

Because φ cannot be expressed as an explicit function of F, we solve numerically for δ_x, δ_y and δ_z by minimizing the following function

$$f(\delta_x, \delta_y, \delta_z) = \sqrt{(\delta_a - \delta_A)^2 + (\theta_a - \theta_A)^2 + (\delta_b - \delta_B)^2 + (\theta_b - \theta_B)^2} \tag{4.5}$$

*Note that $\mathbf{u}$ and $-\mathbf{u}$ would be interchangeable for our purposes

where

$$\begin{aligned}
\delta_a &= \delta' \cdot F\left(\arctan\left(\frac{\delta_z}{\sqrt{\delta_x^2+\delta_y^2}}\right)\right) \\
\delta_b &= \delta' \cdot F\left(\arctan\left(\frac{(\delta_z\cdot\cos\alpha-\delta_x\sin\alpha)}{\sqrt{(\delta_z\sin\alpha+\delta_x\cos\alpha)^2+\delta_y^2}}\right)\right) \\
\theta_a &= \arctan\left(\frac{\delta_y}{\delta_x}\right) \\
\theta_b &= \arctan\left(\frac{\delta_y}{(\delta_z\sin\alpha+\delta_x\cos\alpha)}\right)
\end{aligned} \tag{4.6}$$

Various versions of this function (Eq. 4.5) were tested for different simulated axis orientations and were found to yield varying levels or accuracy/reliability for magnitude ($\delta' = \sqrt{\delta_x^2+\delta_y^2+\delta_z^2}$) and axis ($\mathbf{u} = (\delta_x, \delta_y, \delta_z)/\delta'$). The form described by Eq. 4.5 was determined to yield the best combined reliability and was therefore used for all reconstructions presented here.

4.2.4 Performance metrics

The reliability of the dual projection reconstruction method was assessed separately for the magnitude and the orientation of the reconstructed linear retardance. For each value of reconstructed linear retardance, the magnitude was compared to the average reconstructed linear retardance to find the relative deviation $\Delta\delta'_i = |\delta'_i - \bar{\delta}'|/\bar{\delta}'$ where δ'_i is the magnitude of the reconstructed linear retardance, and $\bar{\delta}'$ is the average over all reconstructed points, which is taken as a measure of the "true" linear retardance (see discussion in Section 4.3.2). The angle error $0 \leq \beta \leq 90°$ between the known anisotropy axis and the axis found from the reconstruction was taken as a measure of the accuracy of the reconstructed axis direction.

4.3 Results

4.3.1 Effect of anisotropy axis orientation on measured values

Figure 4.4 shows the apparent (measured) linear retardance δ_{app} for different values of the elevation angle (φ in Fig. 4.3), with points in each 10° interval being averaged together. The apparent linear retardance of the polystyrene sphere follows the theoretical curve (Eqs. 4.1-4.2) until the elevation angle φ reaches approximately 70°, at which point the measured linear retardance plateaus around $\delta_{app} = 6°$. This is most likely due to noise (the lowest measured values in any sample are on the order of 2-3°). For no position of the sphere did the transmission through crossed polarizers vanish completely (as it would be expected to when the anisotropy axis and probing beam are parallel): this could be due to imprecision in the positioning or alignement of the polarizers, or to ambient light scattering off of the sphere. Note that there is no significant difference in behaviour for the on-axis ($\chi = 0°$) and off-axis ($\chi = 8°$) results.

If we approximate the mean pathlength of photons through the sphere to be 8 mm and use $\delta_{app} = 41°$ and $F(\varphi = 0) = 1$, we can obtain an estimate of the real birefringence: $\Delta n = 9.0 \times 10^{-6} \approx 1 \times 10^{-5}$. Considering the index of refraction of polystyrene is 1.55-1.59, we find that $n_e/n_o \approx 1 + 0.66 \times 10^{-5}$, which is close enough to our input value of $n_e/n_o = 1.001$ (see Section 4.1).

4.3.2 Performance of dual projection reconstructions

Dual projection reconstructions were performed for 39 different positions of the sphere (19 reconstructions with the on-axis incident beam, and 20 reconstructions with the off-axis incident beam). The average angle error for all positions is $\bar{\beta} = 9.0° \pm 8.5°$, which shows good agreement between the reconstructed axis and known anisotropy axis. The average reconstructed linear retardance is $\bar{\delta'} = 41.4° \pm 7.5°$. Note that the average recon-

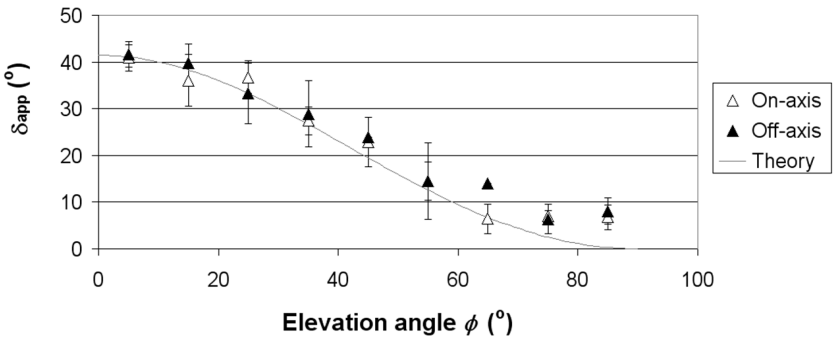

Figure 4.4: Effect of elevation angle φ on apparent linear retardance. Error bars = standard deviation.

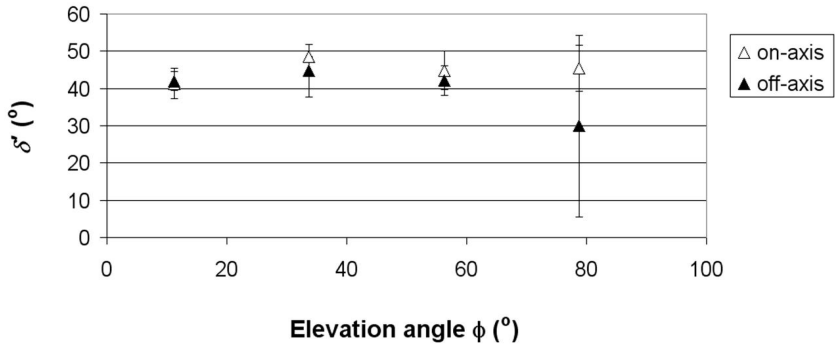

Figure 4.5: Reconstructed linear retardance values for different elevation angle φ values. Error bars = standard deviation.

structed linear retardance corresponds quite well to the apparent linear retardance for the case where the anisotropy axis of the sphere is perpendicular to the probing beam, when we expect $F(\varphi = 0) = 1$ and $\delta_{app} = \delta'$: the six measurements which satisfy this criterium have a mean value of $41.8° \pm 4.3°$ (compared to $\bar{\delta}' = 41.4° \pm 7.5°$).

Figure 4.5 shows the reconstructed linear retardance values for different elevation angles. We find that the reconstructed values are a much more constant representation of anisotropy than the apparent linear retardance (see Fig. 4.4), especially in the case of on-axis measurements. For off-axis measurements, the high elevation angles result in a larger error.

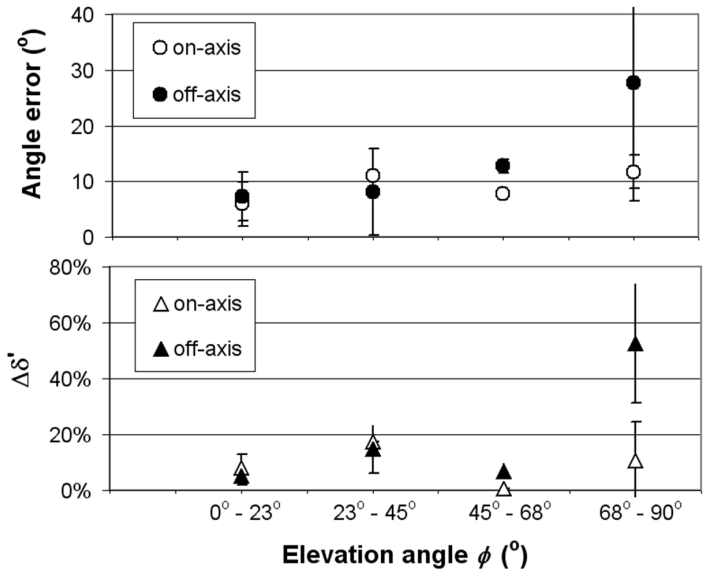

Figure 4.6: Effect of elevation angle φ on reconstruction performance. Error bars = standard deviation.

4.3.3 Effect of anisotropy axis orientation on reconstruction

The first parameter expected to have an effect on the performance of the reconstruction is the elevation angle φ. The results shown in Figure 4.6 reveal that the magnitude of the reconstructed linear retardance and the orientation of the anisotropy axis are relatively consistent for all reconstructions in the on-axis ($\chi = 0°$) group, with an average relative deviation $\Delta\delta'$ of just under 10% and angle error β between $5° - 15°$. For the off-axis ($\chi = 8°$) measurements, a significantly larger error appears for values of $\varphi >\approx 70°$, with $\beta \geq 25°$ and $\delta' \geq 50\%$. (Note that there was no trend as to whether the magnitude was higher or lower than average). This is consistent with our expectations: results from Fig. 4.4 suggest that δ_{app} deviates from theory for $\varphi >\approx 70°$, at which point the reconstruction (which relies the theoretical relationship between δ_{app} and φ) would be expected to break down because of poor signal-to-noise ratio. This does not happen for the on-axis measurements, perhaps because of a better signal-to-noise ratio (due to higher polarization retention, for instance).

Unexpectedly, the degree to which the axis orientation was aligned with the y-axis (see Fig. 4.3) was found to also have an effect on the performance of the reconstruction. Figure 4.7 shows the angle error and relative deviation as a function of the y-component of the sphere's anisotropy axis orientation $u_y = \delta_y/\delta'$. Note that only points for which $\varphi \leq 60°$ were used in Fig. 4.7, so as not to confound these effects with those of a large value of the elevation angle.

While the relative deviation $\Delta\delta'$ seems to be independent of the y-component (with values roughly $5° \leq \Delta\delta' \leq 10\%$) for off-axis measurements, the angle error β decreases with increasing y-component: the points with highest y-component (0.85-1.00) have an angle error of $\beta < 4°$ but the points with smallest y-component (0.00-0.15) have an angle error of $\beta > 12°$. Note that this error is smaller than that resulting from a high elevation angle ($\varphi \geq 70°$) (see Fig. 4.6). One possible source for this error is the fact that the y-axis is the rotation axis between the two sphere positions needed for each reconstruction: because of this, any error on the value of α would have little effect on the reconstruction of a vector lying parallel to the y-axis. Another possibly more important cause is that the direction of incidence of the incoming probing beam has been rotated around the y-axis for all the off-axis points. While we have up to here referred to the "direction of the probing beam", this is not perfectly exact since the incoming and outgoing beams are not perfectly colinear. For the purposes of our analysis, however, we approximate that the (off-axis) incident beam is parallel to the outgoing beam. However, when the anisotropy axis lies in the xz-plane (perpendicular to the y-axis), the difference between the *approximate* incident-beam-to-anisotropy-axis angle and the *real* incident-beam-to-anisotropy-axis angle is much greater than when the anisotropy axis lies predominantly along the y-axis.

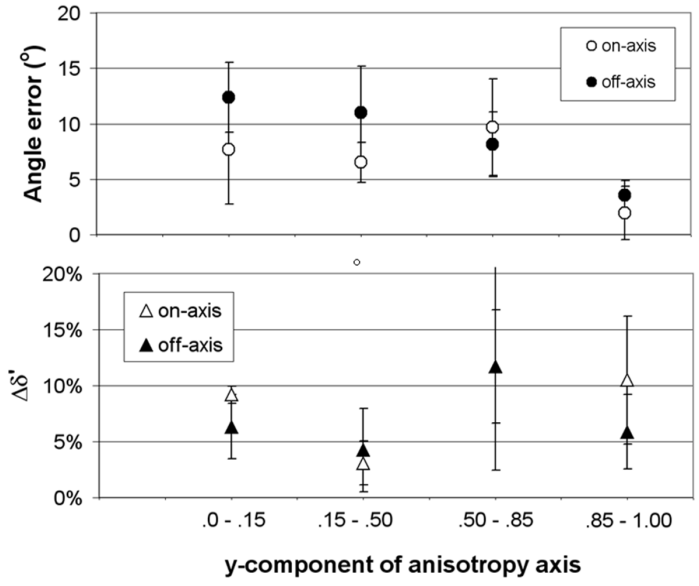

Figure 4.7: Effect of y-component of axis on reconstruction performance. Error bars = standard deviation.

4.3.4 Effect of rotation angle on reconstruction

The value of α (the rotation angle between the two sphere projections required for each reconstruction) was found to have little bearing on the performance of the reconstruction for $15 \leq \alpha \leq 30^\circ$ (see Fig. 4.8). Values of α larger than roughly 30° resulted in large errors and were therefore rejected. Because smaller α angles result in more similar images for thinly-sliced tissue samples (i.e. less distortion of the second imaged due to its slightly rotated position) and therefore better pixel-to-pixel correspondance, it would be interesting to investigate (in future studies) how small we can make α before the performance of the reconstruction starts to suffer.

4.4 Discussion

The results presented here show the efficacy of the dual-projection reconstruction method in overcoming the ambiguity in interpretation of the apparent linear retardance by providing a geometry-independent measure of tissue anisotropy (the reconstructed linear

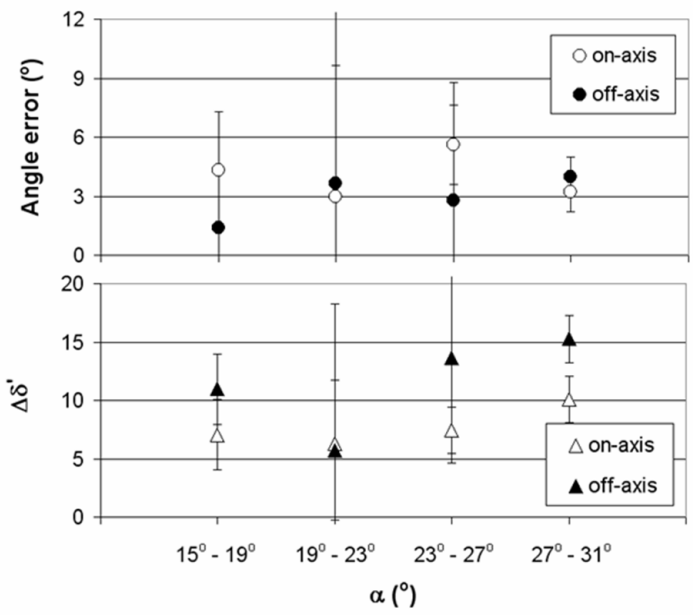

Figure 4.8: Effect of α of axis on reconstruction performance. Error bars = standard deviation.

retardance δ') as well information about the axis of anisotropy. Furthermore, this detailed analysis of the reconstruction performance can provide insight into how to design experimental studies to minimize error. Specifically, whenever possible, we should avoid aligning the anisotropy axis of the material with the probing beam, as well as try to align it with the y-axis when possible, to get minimal error in the reconstruction.

Repeating this experiment with multiple different off-axis angles (χ) instead of the single $\chi = 8°$ value used here would allow us to better assess the error introduced by this configuration, as tissue imaging occasionally requires large χ values ($\approx 20°$), depending on the size and shape of the sample. Further studies will also be required to determine how much, if any, improvement can be gained by using more than two projections for the reconstruction, and whether values of $\alpha < 15°$ may improve the performance of the reconstruction for sliced tissue samples. Lastly, it may be possible to increase the accuracy of the reconstruction method at large elevation angles (i.e. $\varphi > 70°$) by using the empirically determined orientation dependence of the apparent linear retardance (see

Fig. 4.4) rather than the theoretical behaviour described by Eq. 4.1.

Finally, there remain formidable challenges associated with polarimetry imaging of non-uniaxial tissues. For the sphere, we could safely assume that the orientation of the axis was constant throughout the sample, but in tissues, it is distinctly possible that the composition of the tissue varies over the thickness (400 μm) of the sample. This would reduce the apparent linear retardance, and give a value of orientation that is roughly the mean of the orientations at different depths. If the tissue axis changes significantly over that thickness, then our results will be erroneous. Small deviations from the uniaxial case, however, should result in a measured value of anisotropy that is only slightly lower than the true value, and an anisotropy axis that would be representative of the average orientation of the sample axis.

4.5 Conclusion

In this chapter we have presented a method for dealing with the ambiguity associated with single-projection polarimetry measurements. By measuring the optical properties of a sample in two different positions with respect to the probing beam, additional information can be obtained about the anisotropy axis of the material, and a geometrically-independent measure of anisotropy can be found. We have presented data from a polystyrene sphere of known anisotropy axis which allowed us to validate and characterize the performance of this method. Specifically, we find that the reconstruction performs best when the anisotropy axis is perpendicular rather than parallel to the probing beam, and lies parallel rather than perpendicular to the y-axis.

Chapter 5

Comparison of polarimetry and diffusion tensor imaging

5.1 Introduction

The dual projection method presented in the last chapter was shown to adequately determine the optical axis and to yield a consistent measure of anisotropy for a polystyrene sphere of known anisotropy axis. It would be useful to verify that it performs as well in more complex, biological samples. Because the anisotropy axis and birefringence of tissue samples cannot be known *a priori*, an independent way of assessing tissue anisotropy and anisotropy axis orientation is needed.

Diffusion-tensor magnetic resonance imaging (DT-MRI) is well suited for this purpose. A well established method used to derive fiber directions as well as parameters like fractional anisotropy (FA)[91], DT-MRI has been validated against histology[92] and shown to provide information about tissue small-scale structure by revealing anisotropy in the diffusivity of water in a tissue. Furthermore, it is known that in the case of myocardial infarction, the site of injury (i.e., the scar) is characterized by a decrease in diffusion

anisotropy, as the collagenous scar tissue replaces the highly fibrillar structure of cardiac muscle[30,31]. Finally, the first eigenvector of the diffusion tensor (corresponding to the direction of the highest diffusion coefficient) is parallel to the direction of the fibers, thus directly revealing the axis of alignment of the muscle fibers.

Thus, DT-MRI can provide an independent measure of anisotropy magnitude (the FA) and of the anisotropy axis (eigenvector of highest eigenvalue) to which to compare the results of the polarimetry dual-projection reconstruction in biological samples. Here, we use pig heart, which because of its larger size is easier to manipulate and more homogenous over small (few millimeters) distances than rat myocardium*.

5.2 Methods

5.2.1 Porcine model of myocardial infarction

The animal model used here is a porcine chronic infarct model; all samples were provided by Mihaela Pop (Graham Wright's group, Sunnybrook Research Institute). All surgical procedures were performed in accordance with Sunnybrook Research Institute (Toronto, Canada) regulations, under an approved Ethical User Agreement protocol. The infarctions were created by 90 minute balloon occlusion of either the left circumflex artery or the left anterior descending artery, followed by reperfusion (flow restoration). The animals were allowed to heal for 6 weeks, which generated chronic infarcts characterized by collagen deposition and formation of fibrous scar tissue, as well as an alteration of fiber architecture and anisotropy, as demonstrated later by histological assessment. The hearts were excised and fixed in formalin, after which DT-MRI was performed. Finally, sections were taken from axial slices in infarcted and non-infarcted regions of the ventricular walls

*This chapter is based in large part on the results that were published in Wallenburg *et al.*[93]

or septum, and were sectioned to 400 μm thick slices in preparation for polarimetry assessment. Confirmatory histopathology was also performed: the whole-mount samples were prepared as in Clarke *et al.*[94] and further were stained with Picrosirius Red, which stains collagen in red and cytoplasm in yellow.

5.2.2 Polarimetry

Polarimetry imaging was performed as described in Section 4.2.2, but with the incident beam arm off-axis by $\chi = 21°$ instead of $\chi = 8°$. The Mueller matrix of the sample was determined for two positions: with the sample plane perfectly perpedicular to the outgoing beam (A), and then rotatated by an angle $12° \leq \alpha \leq 15°$ (depending on the sample) (B). Note that α must be small enough that (i) the photon pathlength through the sample is not changed significantly between the two projections, and (ii) the images recorded by the CCD are similar enough to be registered to one another, despite the slightly different camera perspectives. Mueller matrix decomposition was performed to extract the azimuthal orientations θ_A and θ_B and the apparent linear retardance values δ_A and δ_B, which were then corrected for wrap-around as described in Section 3.2.3. Finally, images A and B were co-registered and dual projection reconstruction (as described in Section 4.2.3) was performed pixel-by-pixel, yielding a reconstructed linear retardance value and a 3D anisotropy axis orientation for each pixel. Note that this method carries the implicit assumption that the tissue orientation is uniaxial and uniform over the thickness of the sample (400 μm).

5.2.3 Diffusion tensor imaging

Preparation of the hearts and diffusion tensor imaging was done by Mihaela Pop from Graham Wright's group (Sunnybrook Research Institute). The excised and fixed (whole) hearts were imaged using a 1.5Tesla Signa GE MR scanner (GE Healthcare, Milwaukee,

WI). Prior to MR imaging studies, the whole hearts were placed in a phantom box filled with Fluorinert, a fluorocarbon-based fluid which has negligible MR signal, for characterization of the fibers' fractional anisotropy. The diffusion-weighted imaging sequence is based on a 3D fast spin echo sequence with diffusion gradients applied in 7 directions, that allows calculation of diffusion tensor[95]. The following MR parameters were used: echo time TE=20-30ms, repetition time TR=700ms, number of excitations NEX=1, b-value = 600, 7 directions for diffusion gradients, with slice thickness = 1.5 mm, a field-of-view and matrix yielding an in-plane interpolated resolution of approximately 0.5 mm x 0.5 mm. Imaging time was approximately 10 hours per heart.

Fractional anisotropy (FA), a measure that describes the degree of anisotropy in the diffusion of water molecules along the myocardial fibers, is given by the following equation:

$$FA = \sqrt{\frac{3}{2}} \frac{\sqrt{(\lambda_1 - \lambda)^2 + (\lambda_2 - \lambda)^2 + (\lambda_3 - \lambda)^2}}{\sqrt{\lambda_1^2 + \lambda_2^2 + \lambda_3^2}} \tag{5.1}$$

where $\lambda_{1,2,3}$ are the eigenvalues of the diffusion tensor, and λ is the mean diffusivity[96]. The FA has values between 0 (isotropic diffusion) and 1 (infinite anisotropy). At each voxel, the FA will give the relative degree of anisotropy, dominated by the largest component (largest eigenvalue of the diffusion tensor). In the case of a cylindrically symmetric anisotropic medium, such as myocardial fibers, $\lambda_1 \gg \lambda_2 = \lambda_3$ and FA ≈ 1. The anisotropy maps (color-coded and/or black and white) were visualized in short axis MRI views with MedINRIA[97] and DTI-Studio[98] software.

5.3 Results

A total of four samples from three different animals were imaged and reconstructed, of which only two are presented here for the sake of conciseness. Figure 5.1 shows two sections taken from the left ventricle of a pig which had undergone left circumflex artery ligation, as well as the corresponding DT-MRI axial slice and histology. The healthy region (a, and green rectangle in c) is taken from the antero-lateral part of the ventricle and is observed to be mostly devoid of collagen (stained red by Picrosirius Red in the histology slice). The infarct region (b, and purple rectangle in c) is taken from the posterior portion of the ventricle (within the left circumflex artery territory) and shows a large area of collagenous scar.

Fig. 5.2 shows the results of Mueller matrix decomposition performed on the 24 images of the healthy sample for positions A and B, after correction for phase wrap-around. There is little variation between the two projections in either the apparent linear retardance δ_{app} or the azimuthal angle θ. Note that the highest values of apparent linear retardance approached 360°; if the photon pathlength is taken to be approximately the same as the thickness of the sample, this corresponds to a maximal birefringence value of 1.6×10^{-3}, which is roughly double the value found by Shoenenberger *et al.*[89]

Figures 5.3 and 5.4 show the optical axis orientation (a) and reconstructed linear retardance (b), as determined by dual projection reconstruction, for the healthy and infarct regions respectively. The anisotropy orientation results are presented in a color-coded display where all directions refer to the axis of the heart: red corresponds to the lateral component of the orientation; green corresponds to the anterior-to-posterior component; and blue corresponds to the superior-to-inferior component. In the healthy region, the alignement of fibers is circumferential, with fibers mostly in the axial plane near the epicardium, but with a gradual shift from the inner to the outer ventricular wall, until the

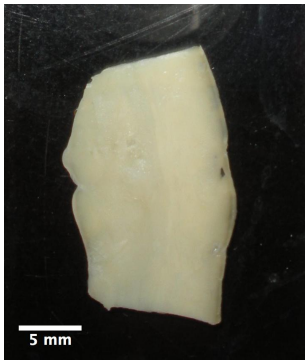

(a) Healthy region

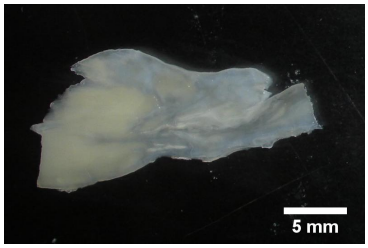

(b) Infarct region

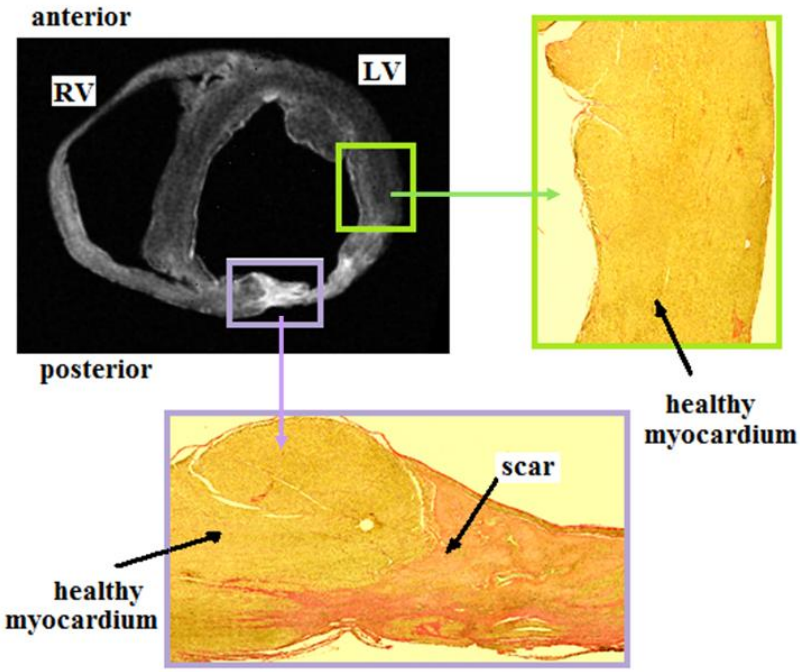

(c)

Figure 5.1: (a) and (b): Photographs of healthy and infarcted regions of the left ventricular wall used for polarimetry imaging. (c) DT-MRI b=0 image (unweighted image, i.e. with no applied diffusion gradient), with histology sections corresponding to healthy and infarcted regions shown in (a) and (b) respectively, stained with Picrosirius Red (collagen in red, cytoplasm in yellow).

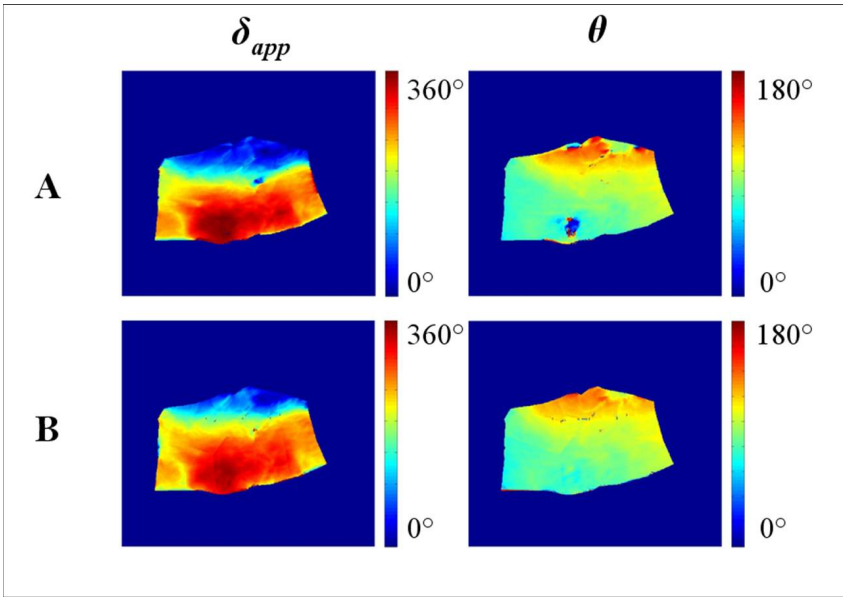

Figure 5.2: Apparent linear retardance (δ_{app}) and azimuthal angle of the anisotropy axis (θ) for a healthy region of porcine myocardium, as measured in two different sample positions (A: perpendicular to probing beam; B: rotated by $\alpha = 12°$), after correction for phase wrap-around. The orientation is measured with respect to the vertical in this image (increasing counter-clockwise).

fibers near the endocardium directed out of the axial plane. This configuration is consistent with the expected double-spiral structure of the heart[4,23] (see also Fig. 2.1c and discussion in Section 2.3). The reconstructed linear retardance varies between 300° and 600° for most of the sample* with the exception of an area of high values (> 600°) near the endocardium (center-left) and an area of very low values (100°-200°) on very inside edge of the endocardium. In the infarct region, the lower left section of the sample shows moderately high values of reconstructed linear retardance (≈ 300°) and a circumferential and roughly axial fiber alignment. However, the majority of the infarct area shows generally low values of reconstructed linear retardance (0°-200°) interspersed with small areas of very high values (> 600°). The low values are consistent with previous cardiac birefringence results that have shown a decrease in tissue anisotropy as healthy cardiac

*Note that while the *reconstructed* linear retardance values exceed 360°, the *apparent* linear retardance remain in the value range of 0°-360° which can be resolved when the phase wrap-around artifact is accounted for.

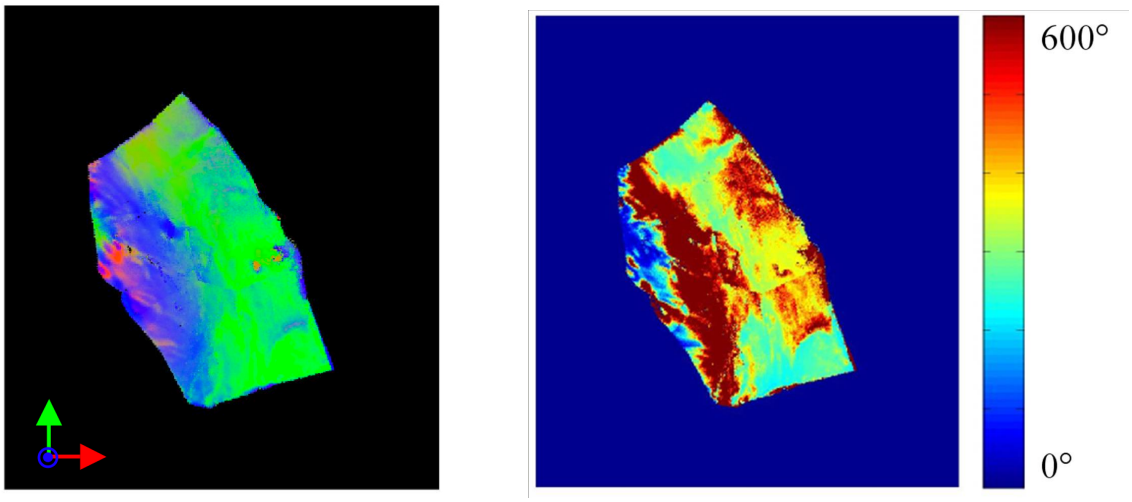

(a) (b)

Figure 5.3: Polarimetry results of anisotropy axis orientation (a) and reconstructed linear retardance (b) for a healthy region of porcine (left ventricular) myocardium, as found with dual projection reconstruction. Color scheme for orientation: lateral component in red; anterior-to-posterior component in green; superior-to-inferior component in blue.

muscle is replaced with infarcted tissue[36,60]. Furthermore, the disrupted aspect of the fiber orientation, which shows an alternance of small areas of axially-oriented and non-axially-oriented tissue instead of the smoother pattern observed in Fig. 5.3 and reflective of double-spiral fiber alignment, suggests severe disruption of the tissue architecture.

Figure 5.5 shows the DT-MRI results for the anisotropy axis (a) and fractional anisotropy (b). Figure 5.5a shows the diffusion tensor image, a color-coded map of the orientation of the primary eigenvector of the diffusion tensor (indicative of the direction of highest diffusion) with the same color-coding as Fig. 5.3a and 5.4a. We find that the fiber alignement in the region corresponding to our healthy sample is, once again, circumferential and roughly axial towards the outside of the ventricular wall and directed out of the plane closer to the inner ventricular wall, a pattern consistent with the double-sprial structure. The infarct region shows a circumferential and axial fiber orientation in the lower left patch, and roughly vertical orientation (blue) for the rest of the region. Figure 5.5b shows the values of fractional anisotropy (FA), as found with

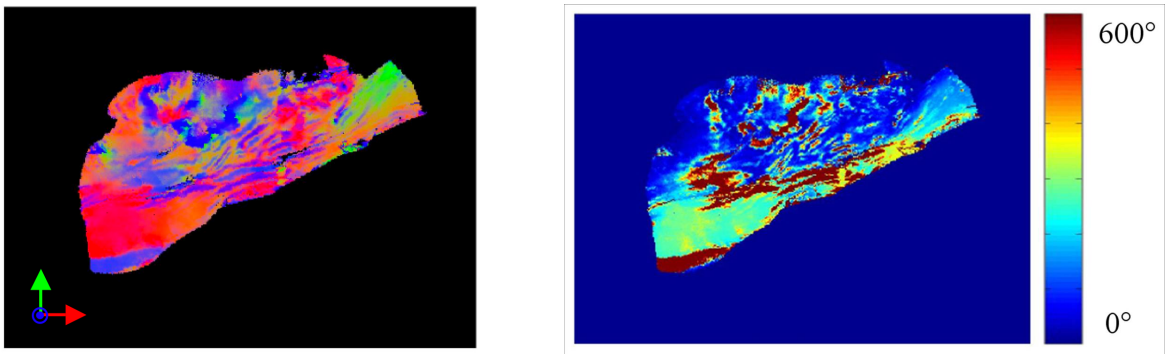

(a) (b)

Figure 5.4: Polarimetry results of anisotropy axis orientation (a) and reconstructed linear retardance (b) for an infarcted region of porcine (left ventricular) myocardium, as found with dual projection reconstruction. Color scheme for orientation: lateral component in red; anterior-to-posterior component in green; superior-to-inferior component in blue.

DT-MRI (see Eq. 5.1): brighter voxels correspond to a higher FA. We find that it is uniformly high in the healthy region, but drops in the infarct region, especially near the inner wall (FA = 0.49±0.19, average ± standard deviation, versus FA = 0.61±0.18 in the healthy region). This is consistent with the findings of many other groups who have also reported decreased FA values in infarcted pig[29], rat[99] and human[30] heart, though one group has reported an increased FA in infarcted mice hearts[100].

Comparison of the DT-MRI orientation image with the polarimetry images (Fig. 5.3a and 5.4a) shows a strong correspondence between the fiber orientations determined with polarimetry and DT-MRI, except where small-scale variations in orientation (as distinguished by polarimetry) are averaged out in the DT-MRI image.

Comparison of the magnitude of the anisotropy, as conveyed by the FA in Fig. 5.5b and the reconstructed linear retardance in Figs. 5.4a-5.4b, reveals reasonable agreement between both methods, as witnesssed by the common trend of lowered anisotropy in corresponding infarct regions, though the reconstructed linear retardance of the healthy region is not as uniform as its FA. Unexpectedly, there is a slow increase in value of

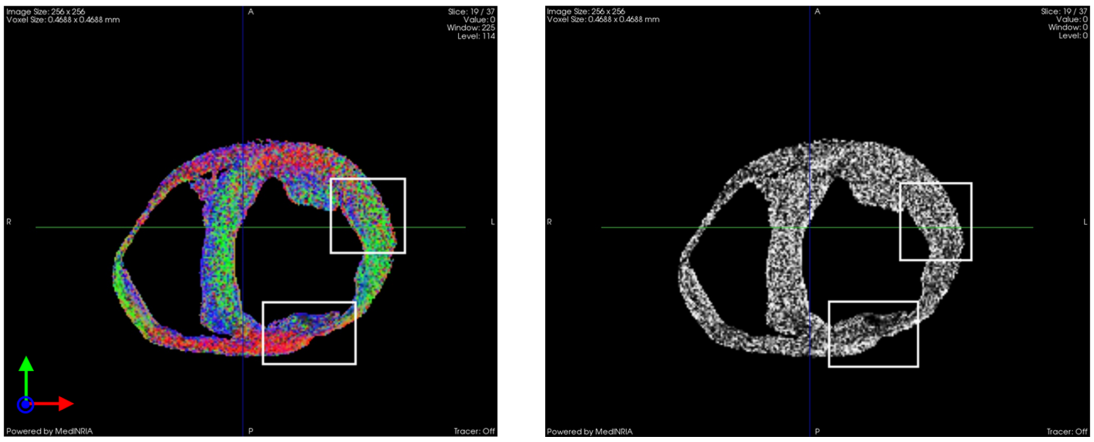

(a) (b)

Figure 5.5: Diffusion tensor imaging results in an infarcted pig heart. (a) Anisotropy axis orientation as found with DT-MRI (primary eigenvector of the diffusion tensor, corresponding to the direction of highest diffusivity). Color scheme: red scale corresponds to lateral component; the green scale corresponds to anterior-to-posterior component; and blue scale corresponds to superior-to-inferior component. (b) Fractional anisotropy (FA) as found with DT-MRI. (Grayscale of FA values between 0 and 1). In both images, white boxes correspond to approximate location of samples used for polarimetry imaging (see Fig. 5.1).

reconstructed linear retardance from the outer to the inner ventricular wall. Comparison of a and b in Fig. 5.3 and 5.4 shows that the voxels presenting very high ($> 600°$) reconstructed linear retardance are all voxels for which the anisotropy axis is almost parallel to the probing beam. This is consistent with our results from Section 4.3.3 which predicted that this alignment of the sample anisotropy axis with the beam would result in poor performance of the reconstruction algorithm. Contrary to Section 4.3.3, however, we find that the reconstructed linear retardance values are systematically overestimated (for the sphere, there was no trend as to whether the reconstructed linear retardance was higher or lower.)

5.4 Discussion

Despite differences in technique and interrogation volume, polarimetry and diffusion tensor MRI show very good agreement for the axis of anisotropy, and reasonable concordance for anisotropy magnitude, except in regions where the dual projection reconstruction performs poorly due to the alignment of the tissue anisotropy axis with the probing beam. The two methods compared here each have respective strengths and weaknesses: DT-MRI does not require sectioning of the heart, which preserves the sample intact *and* allows volumetric, whole-heart imaging. It can also be performed non-invasively *in vivo*[30], albeit with much lower resolutions than those here: the very high resolutions that can be achieved with *ex vivo* imaging require very long scan times (10 hours), while the length of *in vivo* scan times is limited by the duration of a breath-hold and the necessity to gate for cardiac motion. Polarimetry has a higher resolution in the axial plane, with features on the order of $\approx 300\ \mu m$ being clearly distinguishable on both the anisotropy axis and the maximum linear retardance images, but cannot provide as large a field of view (maximum of about 2 cm $\times$ 2 cm). Data acquisition can be done much faster and requires a relatively simple experimental apparatus. However, polarimetry has a limited depth of penetration: some degree of polarization retention is necessary for accurate parameter extraction, limiting the distance that light can travel through depolarizing tissues, and the inability to resolve apparent linear retardance values larger than 360° will also limit the practical depth that can be probed in highly birefringent tissues, e.g. to $\approx 400\mu$m in pig myocardium. Polarimetry is also not volumetric (signal is integrated over the 400 μm thickness of the sample). Note that using a polarization-sensitive optical coherence tomography setup for these measurements would allow depth-resolution of the linear retardance values, which would then circumvent the problem of averaging together optical effects of different tissue layers of potentially different birefringence and orientation.

5.5 Conclusion

Using both polarimetry and DT-MRI, we find that the anisotropy of infarcted pig heart tissue is lower than that of healthy or remote heart tissue, as determined by FA and reconstructed linear retardance. Furthermore, the double-spiral organization of cardiac fibers is destroyed in the infarct regions. Additionally, polarimetry results suggest that the infarct region is highly heterogeneous, with important small-scale changes not detected by DT-MRI because of the larger voxel size. Finally, we have shown that polarimetric assessment of anisotropy and anisotropy axis orientation is consistent with that of diffusion tensor MRI in most cases, with the exception being areas where the fiber orientation and (polarimetric) probing beam are aligned.

Chapter 6

Conclusion

6.1 Summary

The work presented in this thesis has explored the use of two optical methods to assess the state of healthy, infarcted and stem cell treated myocyardium.

The two-photon microscopy results presented in Chapter 2 demonstrate the potential of simultaneous visualization of the collagen and myocyte compartments of infarcted myocardium, using second-harmonic generation and two-photon excitation fluorescence. The findings from two-photon microscopy of infarcted and stem-cell treated rat hearts support the current understanding of the mechanisms of functional improvement by stem cell regeneration, namely that injection of cells into infarcted myocardium improves heart function by limiting necrosis and collagen accumulation.

In Chapter 3, we have shown that polarimetry imaging visualizes injury patterns in the tissue, and comparison to two-photon microscopy has confirmed that measured linear retardance values reflect both the composition (myocytes or collagen) and organization (linear or wavy collagen) of tissue, as well as the alignement of birefringent structures

within the tissue. Results from a polarimetry study comparing two different rat models of infarct suggest that permanent ligation of a cardiac artery results in a more severe and more localized injury to the myocardium than a temporary ligation followed by reperfusion of the tissue.

The experiment presented in Chapter 4 shows that, using dual-projection reconstruction, we can obtain a geometry-independent measure of anisotropy and reliably determine the anisotropy axis orientation. Comparison to diffusion tensor magnetic resonance imaging (Chapter 5), shows the orientations determined with each method agree quite well for most anisotropy axis orientations, and confirms that the dual-projection reconstruction performs poorly when the anisotropy axis and the probing beam are parallel.

We find that each optical method (two-photon microscopy and polarimetry) has advantages and disadvantages. Compared to histology and conventional or confocal microscopy, two-photon microscopy has the advantages of being endogenous (no tissue staining required), having very high resolution and low out-of-plane signal. It is also depth-resolved, and has the potential for volumetric imaging, though this was not exploited here. Unfortunately, while the depth penetration ($\approx 100\mu m$) is high for an optical method, it is still quite low by medical imaging standards (i.e., when compared to ultrasound, magnetic resonance, or nuclear imaging). Finally, two-photon microscopy requires specialized and expensive equipment.

Polarimetry has the advantages of requiring a relatively simple experimental setup. Compared to microscopy techniques, it has a large field of view ($\approx$ 2 cm $\times$ 2 cm) while maintaining a high planar resolution and requires very little tissue processing. However, it has no depth resolution, which is problematic if the birefringence or the anisotropy axis of the tissue varies appreciably over the thickness of the sample. Compared to other

medical imaging techniques, it has high resolution, but a small field of view and poor depth penetration. Finally, even with dual-projection reconstruction, polarimetry cannot determine the exact source of the anisotropy being measured (eg. can't distinguish high birefringence from myocytes or linear collagen).

From a biological perspective, we find that two-photon might be most useful for initial, thorough characterization of the tissues, while polarimetry is perhaps better suited for later studies, once the mechanisms at work have been identified, to quickly characterize larger numbers of samples.

6.2 Future work

The two-photon microscopy work presented here could be expanded towards whole-heart, volumetric data acquisition. This could then yield quantifiable data on collagen/myocyte content (e.g. by volume), organization of collagen (e.g. entropy), etc. and provide better insight into injury and repair mechanisms in infarcted myocardium.

The dual-projection method could be improved upon in a few different ways. The first would be to use the empirically-determined apparent linear retardance behaviour (with noise, see Fig. 4.4) as opposed to the theoretical behaviour (described by Eq. 4.1) in the reconstruction algorithm, potentially resulting in a more accurate value of reconstructed linear retardance at large elevation angles φ. The second would be to use the information from the axis (which is fairly accurate regardless of the elevation angle φ) to correct the reconstructed linear retardance, if it is systematically overestimated by the reconstruction algorithm (as seems to be the case from comparison with DT-MRI results, see Chapter 5). This would require characterizing much more precisely the behaviour of

the reconstructed linear retardance as a function of the value of φ.

The polarimetry work could be extended towards more applications, including potential *in vivo* applications. The first steps in that direction will be to optimize imaging parameters for the backscattering geometry, including the location of the detection position (Monte Carlo studies have shown that in near the exact backscatter direction, scattering-induced effects reduce the accuracy of the Mueller matrix decomposition, but that these effects are reduced for detection positions more than one transport length away from the point of illumination[101]). The backscatter geometry also affects the average pathlength of collected photons[102] and, in preliminary measurements, was found to result in a higher depolarization (which might be mitigated by methods such as optical clearing[103]). Furthermore, automation of the data acquisition would speed up measurements, which will be necessary for most cardiac *in vivo* measurements, while using Mueller matrix decomposition with a polarization-sensitive optical coherence tomography system would allow depth-resolved birefringence measurements .

Finally, the experimental polarimetry and multi-photon imaging methods presented here could be used to investigate other biological applications, for instance to study disease or treatment of non-cardiac muscle, of bones (which have high collagen content and therefore presumably exhibit high birefringence in their healthy state), or of tumors (whose stroma contains collagen).

Bibliography

[1] Statistics Canada, "Mortality, summary list of causes (2005)." Online (consulted June 2010). URL: http://dsp-psd.pqgsc.gc.ca/collection_2009/statcan/84F0209X/84f0209x2005000-eng.pdf

[2] L. H. Opie, *Heart physiology: from cell to circulation.* Lippincott Williams & Wilkins, 4th ed., (2004).

[3] B. Swynghedauw, "Molecular mechanisms of myocardial remodeling," *Physiological Reviews* **79**, p. 215, (1999).

[4] P. Helm, L. Younes, M. Beg, D. Ennis, C. Leclercq, O. Faris, E. McVeigh, D. Kass, M. Miller, and R. Winslow, "Evidence of structural remodeling in the dyssynchronous failing heart," *Circulation Research* **98**, p. 125, (2006).

[5] J. Garot, O. Pascal, B. Diebold, G. Derumeaux, B. Gerber, J. Dubois-Rande, J. Lima, and P. Gueret, "Alterations of systolic left ventricular twist after acute myocardial infarction," *American Journal of Physiology- Heart and Circulatory Physiology* **282**, p. H357, (2002).

[6] J. Wu, F. Zeng, R. Weisel, and R. Li, "Stem cells for cardiac regeneration by cell therapy and myocardial tissue engineering," *Advances in Biochemical Engineering/Biotechnology* **114**, pp. 107–128, (2009).

[7] J. Sam, D. Angoulvant, S. Fazel, R. D. Weisel, and R.-K. Li, "Heart cell implantation after myocardial infarction," *Coronary Artery Disease* **16**, pp. 85–91, (2005).

[8] P. Farahmand, T. Lai, R. Weisel, S. Fazel, T. Yau, P. Menasche, and R. Li, "Skeletal myoblasts preserve remote matrix architecture and global function when implanted early or late after coronary ligation into infarcted or remote myocardium," *Circulation* **118**, p. S130, (2008).

[9] M. S. Penn, ed., *Stem Cells and Myocardial Regeneration*. Humana Press, (2007).

[10] D. Orlic, J. Kajstura, S. Chimenti, I. Jakoniuk, S. M. Anderson, B. Li, J. Pickel, R. McKay, B. Nadal-Ginard, D. M. Bodine, A. Leri, and P. Anversa, "Bone marrow cells regenerate infarcted myocardium," *Nature* **410**, pp. 701–705, (2001).

[11] K. A. Jackson, S. M. Majka, H. Wang, J. Pocius, C. J. Hartley, M. W. Majesky, M. L. Entman, L. H. Michael, K. K. Hirschi, and M. A. Goodell, "Regeneration of ischemic cardiac muscle and vascular endothelium by adult stem cells," *Journal of Clinical Investigation* **107**, p. 1395, (2001).

[12] S. Fazel, D. Angoulvant, J. Butany, R. D. Weisel, and R.-K. Li, "Mesenchymal stem cells engineered to overexpress stem cell factor improve cardiac function but have malignant potential," *Journal of Thoracic and Cardiovascular Surgery* **136**, p. 1388, (2008).

[13] J. Jin, S. I. Jeong, Y. M. Shin, K. S. Lim, H. soo Shin, Y. M. Lee, H. C. Koh, and K.-S. Kim, "Trasmplantation of mesenchymal stem cells within a poly(lactide-co-ϵ-caprolactone) scaffold improves cadriac function in a rat myocardial infarction model," *European Journal of Heart Failure* **11**, pp. 147–153, (2009).

[14] W. Li, N. Ma, L.-L. Ong, C. Nesselmann, C. Klopsch, Y. Ladilov, D. Furlani, C. Piechaczek, J. M. Moebius, K. Lutzow, A. Lendlein, C. Stamm, R.-K. Li, and

G. Steinhoff, "Bcl-2 engineered mscs inhibited apoptosis and improved heart function," *Stem Cells* **25**, pp. 2118–2127, (2007).

[15] A. P. Beltrami, L. Barlucchi, D. Torella, M. Baker, F. Limana, S. Chimenti, H. Kasahara, M. Rota, E. Musso, K. Urbanek, A. Leri, J. Kajstura, B. Nadal-Ginard, and P. Anversa, "Adult cardiac stem cells are multipotent and support myocardial regeneration," *Cell* **114**, pp. 763–776, (2003).

[16] B. Murtuza, K. Suzuki, G. Bou-Gharios, J. Beauchamp, R. Smolenski, T. Partridge, and M. Yacoub, "Transplantation of skeletal myoblasts secreting an IL-1 inhibitor modulates adverse remodeling in infarcted murine myocardium," *Proceedings of the National Academy of Sciences* **101**, p. 4216, (2004).

[17] X. Xie, F. Cao, A. Y. Sheikh, Z. Li, A. J. Connolly, X. Pei, R.-K. Li, R. C. Robbins, and J. C. Wu, "Genetic modification of embryonic stem cells with vegf enhances survival and improves cardiac function," *Cloning and Stem Cells* **9**, p. 549, (2007).

[18] B. M. Carlson, ed., *Stem cell anthology, Chapter 22.* Academic Press Elsevier, (2010).

[19] C. E. Murry, M. H. Soonpaa, H. Reinecke, H. Nakajima, H. O. Nakajima, M. Rubart, K. B. S. Pasumarthi, J. I. Virag, S. H. Bartelmez, V. Poppa, G. Bradford, J. D. Dowell, D. A. Williams, and L. J. Fields, "Maematopoietic stem cells do not transdifferentiate into cardiac myocytes in mycardial infarcts," *Nature* **428**, p. 664, (2004).

[20] P. W. M. Fedak, P. E. Szmitko, R. D. Weisel, S. M. Altamentova, N. Nili, N. Ohno, S. Verma, S. Fazel, B. H. Strauss, and R.-K. Li, "Cell transplantation preserves matrix homeostasis: A novel paracrine mechanism," *Journal of Thoracic and Cardiovascular Surgery* **130**, pp. 1430–1439, (2005).

[21] S. Fazel, M. Cimini, L. Chen, S. Li, D. Angoulvant, P. Fedak, S. Verma, R. D. Weisel, A. Keating, and R.-K. Li, "Cardioprotective c-kit$^+$ cells are from the bone marrow and regulate the myocardial balance of angiogenic cytokines," *Journal of Clinical Investigation* **116**, p. 1865, (2006).

[22] S. Chimenti, E. Carlo, S. Masson, A. Bai, and R. Latini, "Myocardial infarction: animal models," *Methods in Molecular Medicine* **98**, (2004).

[23] P. Sengupta, V. Krishnamoorthy, J. Korinek, J. Narula, M. Vannan, S. Lester, J. Tajik, J. Seward, B. Khandheria, and M. Belohlavek, "Left ventricular form and function revisited: applied translational science to cardiovascular ultrasound imaging," *Journal of the American Society of Echocardiography* **20**, pp. 539–551, (2007).

[24] A. Wagner, H. Mahrholdt, T. A. Holly, M. D. Elliot, M. Regenfus, M. Parker, F. J. Kocke, R. O. Bonow, R. J. Kim, and R. M. Judd, "Contrast-enhanced MRI and routine single photon emission computed tomography (SPECT) perfusion imaging for detection of subendocardial myocardial infarcts: an imaging study," *Lancet* **361**, pp. 374–379, (2003).

[25] R. Malkin, N. Kramer, B. Schnitz, M. Gopalakrishnan, and A. Curry, "Advances in electrical and mechanical cardiac mapping," *Physiological Measurement* **26**, p. R1, (2005).

[26] J. Coletta, N. Rosenthal, and M. Costa, "Cardiac mapping and stem cell delivery for the damaged myocardium," *Expert Review of Cardiovascular Therapy* **6**, pp. 1181–1190, (2008).

[27] M. Attin and W. Clusin, "Basic concepts of optical mapping techniques in cardiac electrophysiology," *Biological Research For Nursing* **11**, p. 195, (2009).

[28] J. Chen, S. Song, W. Liu, M. McLean, J. Allen, J. Tan, S. Wickline, and X. Yu, "Remodeling of cardiac fiber structure after infarction in rats quantified with diffusion tensor MRI," *American Journal of Physiology- Heart and Circulatory Physiology* **285**, p. H946, (2003).

[29] Y. Wu, C. Chan, J. Nicholls, S. Liao, H. Tse, and E. Wu, "MR study of the effect of infarct size and location on left ventricular functional and microstructural alterations in porcine models," *Journal of Magnetic Resonance Imaging* **29**, pp. 305–312, (2009).

[30] M. Wu, W. Tseng, M. Su, C. Liu, K. Chiou, V. Wedeen, T. Reese, and C. Yang, "Diffusion tensor magnetic resonance imaging mapping the fiber architecture remodeling in human myocardium after infarction: correlation with viability and wall motion," *Circulation* **114**, p. 1036, (2006).

[31] E. Wu, Y. Wu, H. Tang, J. Wang, J. Yang, M. Ng, E. Yang, C. Chan, S. Zhu, C. Lau, *et al.*, "Study of myocardial fiber pathway using magnetic resonance diffusion tensor imaging," *Magnetic Resonance Imaging* **25**, pp. 1048–1057, (2007).

[32] M. Matsumoto-Ida, M. Akao, T. Takeda, M. Kato, and T. Kita, "Real-time 2-photon imaging of mitochondrial function in perfused rat hearts subjected to ischemia/reperfusion," *Circulation* **114**, p. 1497, (2006).

[33] W. Hucker, C. Ripplinger, C. Fleming, V. Fedorov, A. Rollins, and I. Efimov, "Bimodal biophotonic imaging of the structure-function relationship in cardiac tissue," *Journal of Biomedical Optics* **13**, p. 054012, (2008).

[34] C. Ambrosi, N. Moazami, A. Rollins, and I. Efimov, "Virtual histology of the human heart using optical coherence tomography," *Journal of Biomedical Optics* **14**, p. 054002, (2009).

[35] M. Ogawa, Y. Harada, Y. Yamaoka, K. Fujita, H. Yaku, and T. Takamatsu, "Label-free biochemical imaging of heart tissue with high-speed spontaneous raman microscopy," *Biochemical and Biophysical Research Communications* **382**, pp. 370–374, (2009).

[36] N. Ghosh, M. F. G. Wood, S. Li, R. D. Weisel, B. C. Wilson, R. K. Li, and I. A. Vitkin, "Mueller matrix decomposition for polarized light assessment of biological tissues," *Journal of Biophotonics* **2**, pp. 145–156, (2009).

[37] J. Scherschel and M. Rubart, "Cardiovascular imaging using two-photon microscopy," *Microscopy and Microanalysis* **14**, pp. 492–506, (2008).

[38] M. Oheim, D. J. Michael, M. Geisbauer, D. Madsen, and R. Chow, "Principles of two-photon excitation fluorescence microscopy and other nonlinear imaging approaches," *Advanced Drug Delivery Reviews* **58**, pp. 788–808, (2006).

[39] K. Schenke-Layland, I. Riemann, U. Stock, and K. Konig, "Imaging of cardiovascular structures using near-infrared femtosecond multiphoton laser scanning microscopy," *Journal of Biomedical Optics* **10**, p. 024017, (2005).

[40] A. Zoumi, X. Lu, G. Kassab, and B. Tromberg, "Imaging coronary artery microstructure using second-harmonic and two-photon fluorescence microscopy," *Biophysical Journal* **87**, pp. 2778–2786, (2004).

[41] W. Zipfel, R. Williams, R. Christie, A. Nikitin, B. Hyman, and W. Webb, "Live tissue intrinsic emission microscopy using multiphoton-excited native fluorescence and second harmonic generation," *Proceedings of the National Academy of Sciences of the United States of America* **100**, p. 7075, (2003).

[42] R. Williams, W. Zipfel, and W. Webb, "Interpreting second-harmonic generation images of collagen I fibrils," *Biophysical Journal* **88**, pp. 1377–1386, (2005).

[43] D. Dombeck, K. Kasischke, H. Vishwasrao, M. Ingelsson, B. Hyman, and W. Webb, "Uniform polarity microtubule assemblies imaged in native brain tissue by second-harmonic generation microscopy," *Proceedings of the National Academy of Sciences of the United States of America* **100**, pp. 7081–7086, (2003).

[44] S. Wallace, J. Morrison, K. Botting, and T. Kee, "Second-harmonic generation and two-photon-excited autofluorescence microscopy of cardiomyocytes: quantification of cell volume and myosin filaments," *Journal of Biomedical Optics* **13**, p. 064018, (2008).

[45] S. Plotnikov, A. Millard, P. Campagnola, and W. Mohler, "Characterization of the myosin-based source for second-harmonic generation from muscle sarcomeres," *Biophysical Journal* **90**, pp. 693–703, (2006).

[46] S. Plotnikov, A. Kenny, S. Walsh, B. Zubrowski, C. Joseph, V. Scranton, G. Kuchel, D. Dauser, M. Xu, C. Pilbeam, D. J. Adams, R. P. Dougherty, P. J. Campagnola, and W. A. Mohler, "Measurement of muscle disease by quantitative second-harmonic generation imaging," *Journal of Biomedical Optics* **13**, p. 044018, (2008).

[47] T. Ragan, J. Sylvan, K. Kim, H. Huang, K. Bahlmann, R. Lee, and P. So, "High-resolution whole organ imaging using two-photon tissue cytometry," *Journal of Biomedical Optics* **12**, p. 014015, (2007).

[48] H. Huang, C. MacGillivray, H. Kwon, J. Lammerding, J. Robbins, R. Lee, and P. So, "Three-dimensional cardiac architecture determined by two-photon microtomy," *Journal of Biomedical Optics* **14**, p. 044029, (2009).

[49] K. Schenke-Layland, U. Stock, A. Nsair, J. Xie, E. Angelis, C. Fonseca, R. Larbig, A. Mahajan, K. Shivkumar, M. Fishbein, and W. MacLellan, "Cardiomyopathy is associated with structural remodelling of heart valve extracellular matrix," *European Heart Journal* **30**, p. 2254, (2009).

[50] M. Tsai, Y. Chiou, and C. Sun, "Second harmonic generation imaging of the collagen in myocardium for atrial fibrillation diagnosis," in *Proceedings of SPIE*, vol. 7161, p. 71612O, (2009).

[51] Y. R. Shen, "Surface properties probed by second-harmonic and sum-frequency generation," *Nature* **337**, pp. 519–525, (1989).

[52] P. Campagnola, M.-D. Wei, A. Lewis, and L. M. Loew, "High-resolution nonlinear optical imaging of live cells by second harmonic genearation," *Biophysical Journal* **77**, pp. 3341–3349, (1999).

[53] P. Campagnola, A. Millard, M. Terasaki, P. Hoppe, C. Malone, and W. Mohler, "Three-dimensional high-resolution second-harmonic generation imaging of endogenous structural proteins in biological tissues," *Biophysical Journal* **82**, pp. 493–508, (2002).

[54] J. De Boer, T. Milner, M. van Gemert, and J. Nelson, "Two-dimensional birefringence imaging in biological tissue by polarization-sensitive optical coherence tomography," *Optics Letters* **22**, pp. 934–936, (1997).

[55] B. Park, C. Saxer, S. Srinivas, J. Nelson, and J. de Boer, "In vivo burn depth determination by high-speed fiber-based polarization sensitive optical coherence tomography," *Journal of Biomedical Optics* **6**, p. 474, (2001).

[56] S. Jacques, J. Ramella-Roman, and K. Lee, "Imaging skin pathology with polarized light," *Journal of Biomedical Optics* **7**, pp. 329–340, (2002).

[57] J. Ramella-Roman, K. Lee, S. Prahl, and S. Jacques, "Design, testing, and clinical studies of a handheld polarized light camera," *Journal of Biomedical Optics* **9**, p. 1305, (2004).

[58] S. J. Matcher, "A review of some recent developments in polarization-sensitive optical imaging techniques for the study of articular cartilage," *Journal of Applied Physics* **105**, p. 102041, (2009).

[59] J. Bueno and M. Campbell, "Polarization properties of the in vitro old human crystalline lens," *Ophthalmic and Physiological Optics* **23**, pp. 109–118, (2003).

[60] M. F. G. Wood, N. Ghosh, M. A. Wallenburg, S. Li, R. D. Weisel, B. C. Wilson, R. K. Li, and I. A. Vitkin, "Polarization birefringence measurements for characterizing the myocardium, including healthy, infarcted, and stem cell treated regenerating cardiac tissues," *Journal of Biomedical Optics (in press)* **15**, (2010).

[61] S. Lu and R. Chipman, "Interpretation of mueller matrices based on polar decomposition," *Journal of the Optical Society of America A* **13**, pp. 1106–1113, (1996).

[62] N. Ghosh, M. Wood, and I. A. Vitkin, "Mueller matrix decomposition for extraction of individual polarization parameters from complex media exhibiting multiple scattering, optical activity, and linear birefringence," *Journal of Biomedical Optics* **13**, p. 044036, (2008).

[63] Z. Tannous, M. Al-Arashi, S. Shah, and A. N. Yaroslavsky, "Delineating melanoma using multimodal polarized light imaging," *Lasers in Surgery and Medicine* **41**, pp. 10–16, (2009).

[64] M. van Turnhout, S. Kranenbarg, and J. van Leeuwen, "Modeling optical behavior of birefringent biological tissues for evaluation of quantitative polarized light microscopy," *Journal of Biomedical Optics* **14**, p. 054018, (2009).

[65] N. Ugryumova, J. Jacobs, M. Bonesi, and S. J. Matcher, "Novel optical imaging technique to determine the 3-D orientation of collagen fibers in cartilage: variable-incidence angle polarization-sensitive optical coherence tomography," *Osteoarthiritis and Cartilage* **17**, pp. 33–43, (2009).

[66] X. Li and G. Yao, "Mueller matrix decomposition of diffuse reflectance imaging in skeletal muscle," *Applied Optics* **48**, p. 2625, (2009).

[67] P. Jouk, A. Mourad, V. Milisic, G. Michalowicz, A. Raoult, D. Caillerie, and Y. Usson, "Analysis of the fiber architecture of the heart by quantitative polarized light microscopy. accuracy, limitations and contribution to the study of the fiber architecture of the ventricles during fetal and neonatal life," *European Journal of Cardio-Thoracic Surgery* **31**, pp. 916–922, (2007).

[68] M. A. Wallenburg, J. Wu, R. K. Li, and I. A. Vitkin, "Two-photon microscopy of healthy, infarcted and stem-cell treated regenerating myocardium," *Journal of Biophotonics (accepted)*, (2010).

[69] D. Sun, C. Martinez, O. Ochoa, L. Ruiz-Willhite, J. Bonilla, V. Centonze, L. Waite, J. Michalek, L. McManus, and P. Shireman, "Bone marrow-derived cell regulation of skeletal muscle regeneration," *The FASEB Journal* **23**, p. 382, (2009).

[70] T. Yasui, Y. Tohno, and T. Araki, "Characterization of collagen orientation in human dermis by two-dimensional second-harmonic-generation polarimetry," *Journal of Biomedical Optics* **9**, p. 259, (2004).

[71] G. Cox, E. Kable, A. Jones, I. Fraser, F. Manconi, and M. Gorrell, "3-dimensional imaging of collagen using second harmonic generation," *Journal of Structural Biology* **141**, pp. 53–62, (2003).

[72] E. Brown, T. McKee, E. diTomaso, A. Pluen, B. Seed, Y. Boucher, and R. Jain, "Dynamic imaging of collagen and its modulation in tumors in vivo using second-harmonic generation," *Nature Medicine* **9**, pp. 796–800, (2003).

[73] A. Pope, G. Sands, B. Smaill, and I. LeGrice, "Three-dimensional transmural organization of perimysial collagen in the heart," *American Journal of Physiology-Heart and Circulatory Physiology* **295**, p. H1243, (2008).

[74] G. Bub, P. Camelliti, C. Bollensdorff, D. J. Stuckey, G. Picton, R. A. B. Burton, K. Clarke, and P. Kohl, "Measurement and analysis of sarcomere length in rat cardiomyocytes in situ," *American Journal of Physiology- Heart and Circulatory Physiology* **298**, pp. H1616–H1625, (2010).

[75] M. Both, M. Vogel, O. Friedrich, F. von Wegner, T. Kunsting, R. H. A. Fink, and D. Uttenweiler, "Second harmonic imaging of intrinsic signals in muscle fibers in situ," *Journal of Biomedical Optics* **9**, pp. 882–892, (2004).

[76] I. Freund, M. Deutsch, and A. Sprecher, "Connective tissue polarity: Optical second-harmonic microscopy, crossed-beam summation, and small-angle scattering in rat-tail tendon," *Biophysical Journal* **50**, pp. 693–712, (1986).

[77] J. De Boer, T. Milner, and J. Nelson, "Determination of the depth-resolved stokes parameters of light backscattered from turbid media by use of polarization-sensitive optical coherence tomography," *Optics Letters* **24**, pp. 300–302, (1999).

[78] S. Jiao, G. Yao, and L. Wang, "Depth-resolved two-dimensional Stokes vectors of backscattered light and Mueller matrices of biological tissue measured with optical coherence tomography," *Applied Optics* **39**, pp. 6318–6324, (2000).

[79] C. Sun, L. Lu, C. Yang, and Y. Kiang, "Myocardial tissue characterization based on the time-resolved Stokes-Mueller formalism," *Optics Express* **10**, p. 1347, (2002).

[80] A. Pravdin, D. Yakovlev, A. Spivak, and V. Tuchin, "Mapping of optical properties of anisotropic biological tissues," in *Proceedings of SPIE*, vol. 5695, p. 303, (2005).

[81] M. Smith, "Interpreting mueller matrix images of tissues," in *Proceedings of SPIE*, vol. 4257, p. 82, (2001).

[82] Y. Yasuno, S. Makita, Y. Sutoh, M. Itoh, and T. Yatagai, "Birefringence imaging

of human skin by polarization-sensitive spectral interferometric optical coherence tomography," *Optics Letters* **27**, pp. 1803–1805, (2002).

[83] C. Wu, Y. Wang, L. Lu, C. Sun, C. Lu, M. Tsai, and C. Yang, "Tissue birefringence of hypercholesterolemic rat liver measured with polarization-sensitive optical coherence tomography," *Journal of Biomedical Optics* **12**, p. 064022, (2007).

[84] B. Liu, M. Harman, S. Giattina, D. Stamper, C. Demakis, M. Chilek, S. Raby, and M. Brezinski, "Characterizing of tissue microstructure with single-detector polarization-sensitive optical coherence tomography," *Applied Optics* **45**, pp. 4464–4479, (2006).

[85] J. Wu, Z. Sun, S. Li, H. C. Kuo, G. Michal, S. Basu, G. Chan, E. Madrusov, F. Ludwig, M. A. Wallenburg, I. A. Vitkin, and R. K. Li, "Comparison of long-term structural and functional outcomes of cardiac ischemia/reperfusion and permanent ligation injuries in rat," *(in preparation)*, (2010).

[86] E. Hecht, *Optics*. Addison-Wesley, (2001).

[87] M. F. G. Wood, X. Guo, and I. A. Vitkin, "Polarized light propagation in multiply scattering media exhibiting both linear birefringence and optical activity: Monte carlo model and experimental methodology," *Journal of Biomedical Optics* **12**, p. 014029, (2007).

[88] N. Ghosh, M. F. G. Wood, and I. A. Vitkin, "Influence of the order of the constituent basis matrices on the mueller matrix decomposition-derived polarization parameters in complex turbid media such as biological tissues," *Optics Communications* **283**, pp. 1200–1208, (2010).

[89] K. Schoenenberger, B. Colston, D. Maitland, L. Da Silva, and M. Everett, "Mapping of birefringence and thermal damage in tissue by use of polarization-sensitive optical coherence tomography," *Applied Optics* **37**, pp. 6026–6035, (1998).

[90] M. A. Wallenburg, M. Wood, N. Ghosh, and A. Vitkin, "Polarimetry-based method to extract geometry independent metrics of tissue anisotropy," *Optics Letters* **35**, p. 2570, (2010).

[91] D. Le Bihan and P. van Zijl, "From the diffusion coefficient to the diffusion tensor," *NMR in Biomedicine* **15**, pp. 431–434, (2002).

[92] A. Holmes, D. Scollan, and R. Winslow, "Direct histological validation of diffusion tensor MRI in formaldehyde-fixed myocardium," *Magnetic Resonance in Medicine* **44**, pp. 157–161, (2000).

[93] M. A. Wallenburg, M. Pop, M. F. G. Wood, N. Ghosh, G. A. Wright, and I. A. Vitkin, "Comparison of optical polarimetry and diffusion tensor MR imaging for assessing myocardial anisotropy," *Journal of Innovative Optical Health Sciences* **3**, pp. 109–121, (2010).

[94] G. Clarke, S. Eidt, L. Sun, G. Mawdsley, J. Zubovits, and M. Yaffe, "Whole-specimen histopathology: a method to produce whole-mount breast serial sections for 3-D digital histopathology imaging," *Histopathology* **50**, pp. 232–242, (2007).

[95] P. Helm, H. Tseng, L. Younes, E. McVeigh, and R. Winslow, "Ex vivo 3D diffusion tensor imaging and quantification of cardiac laminar structure diffusion tensor imaging and quantification of cardiac laminar structure," *Magnetic Resonance in Medicine* **54**, p. 850, (2005).

[96] M. Denis Le Bihan, J. Mangin, C. Poupon, C. Clark, S. Pappata, N. Molko, and M. Hughes Chabriat, "Diffusion tensor imaging: concepts and applications," *Journal of Magnetic Resonance Imaging* **13**, pp. 534–546, (2001).

[97] P. Fillard, N. Toussaint, and X. Pennec, "Medinria: DT-MRI processing and visualization software," in *Similar Tensor Workshop*, vol. 5, p. 7, (2006).

[98] H. Jiang, P. van Zijl, J. Kim, G. Pearlson, and S. Mori, "DtiStudio: resource program for diffusion tensor computation and fiber bundle tracking," *Computer Methods and Programs in Biomedicine* **81**, pp. 106–116, (2006).

[99] J. Chen, S.-K. Song, W. Liu, M. McLean, J. S. Allen, J. Tan, S. A. Wickline, and X. Yu, "Remodeling of cardiac fiber structure after infarction in rats quantified with diffusion tensor mri," *American Journal of Physiology - Heart and Circulatory Physiology* **285**, pp. H946–H954, (2003).

[100] G. Strijkers, A. Bouts, W. M. Blankesteijn, T. H. J. Peeters, A. Vilanova, M. C. van Prooijen, H. M. H. F. Sanders, E. Heijman, and K. Nicolay, "Diffusion tensor imaging of left ventricular remodeling in response to myocardial infarction in the mouse," *NMR in Biomedicine* **22**, pp. 182–190, (2008).

[101] N. Ghosh, M. F. G. Wood, and I. A. Vitkin, "Polarimetry in turbid, birefringent, optically active media: A monte carlo study of mueller matrix decomposition in the backscattering geometry," *Journal of Applied Physics* **105**, p. 102023, (2009).

[102] X. Guo, M. F. G. Wood, and I. A. Vitkin, "Stokes polarimetry in multiply scattering chiral media: effects of experimental geometry," *Applied optics* **46**, pp. 4491–4500, (2007).

[103] V. Tuchin, "Optical clearing of tissues and blood using the immersion method," *Journal of Physics D: Applied Physics* **38**, p. 2497, (2005).